FEM INVESTIGATION OF CRACKING DURING CONTINUOUS CASTING

FINITE ELEMENT MODELLING INVESTIGATION OF TRANSVERSE CRACKING DURING CONTINUOUS CASTING OF STEEL

BY

COLE BECKER

B.Eng.(Materials Science & Engineering)

McMaster University

A THESIS

SUBMITTED TO THE DEPARTMENT OF MATERIALS SCIENCE & ENGINEERING

AND THE SCHOOL OF GRADUATE STUDIES

OF MCMASTER UNIVERSITY

IN PARTIAL FULFILMENT OF THE REQUIREMENTS

FOR THE DEGREE OF

MASTER OF APPLIED SCIENCE

Master of Applied Science (2022) McMaster University

(Materials Science & Engineering) Hamilton, Ontario, Canada

TITLE:	Finite Element Modelling Investigation of Transverse Cracking During Continuous Casting of Steel
AUTHOR:	Cole Becker B.Eng.(Materials Science & Engineering) McMaster University
SUPERVISOR:	Professor André Phillion
NUMBER OF PAGES:	xvi, 105

Abstract

Continuous casting represents 96% of all steel products made worldwide. To cast new alloys, optimal process parameters must be determined that reduce quality issues. Traditionally, this is a time-consuming and expensive process due to the need to run multiple casting trials. Alternatively, numerical models can be used to help guide development of optimal process parameters. In this thesis, a 3D thermal-solute-mechanical finite element model has been created using the THERCAST software to simulate the casting process of a new advanced high strength steel grade at Stelco's Lake Erie Works facility. The model represents the caster from mould to exit, and takes into account heat transfer from the mould, sprays, rolls, and ambient air. The model has been extensively validated using plant measurements from steel shim trials and pyrometer data. The model is used to investigate the evolution of temperature and shell thickness along the cast length, and the effect of spray cooling and casting speed on the surface temperature at unbending to predict transverse cracking during secondary cooling. It was found that the susceptibility to cracking increased with lower casting speed and increased water spray cooling. Increasing the casting speed had a negligible effect, and it was found to decrease with decreasing water spray cooling. This decreased water spray cooling is also accompanied by an increase in

metallurgical length, so further work is required to determine appropriate safety factors to ensure the steel is completely solidified. However, preliminary results of solute and mechanical models are also presented. Further work is required to improve the predictions made by these simulations.

Keywords : Transverse cracking, Steel slab, 3D finite element, Finite element analysis, Thermal modelling, Segregation, Mechanical modelling, Stress

This thesis is dedicated to my father for all his love and support.

Acknowledgements

I would like to express my deepest appreciation to my supervisor Dr. André Phillion for his guidance and support. His extensive knowledge of solidification and process metallurgy helped shape this thesis.

I would like to thank my committee member Dr. Oleg Rubel for providing me with great suggestions during my MASc. I would also like to thank my industrial sponsors Chad Cathcart and Serena Morgante from Stelco for their aid. I would also like to extend my appreciation to Dr. Joydeep Sengupta and Jackie Leung for their support and for starting me on this journey.

My gratitude also goes to my friends Javier Miranda, Neil McClean, and Alessandra Merlo, as well as everyone in the SIM3P research group. Their help and friendship have been invaluable throughout my MASc.

Finally, I would like to thank my father for all his love, support, and encouragement throughout.

Contents

Abstract **iii**

Acknowledgements **vi**

Notation, Definitions, and Abbreviations **xiv**

1 Introduction **1**

1.1 Overview 1

1.2 Background of AHSSs 2

1.3 Overview of Casting Process 7

1.4 Outline 9

2 Literature Review **11**

2.1 Introduction 11

2.2 Solidification 12

2.3 Defects in Continuous Casting 14

2.4 Modelling 24

2.5 Use of a Model for Industrial Applications 33

3 Scope & Objectives **34**

4 Methods **36**

4.1 Introduction 36

4.2 Model Formulation, Domain, and Geometry 37

4.3 Thermal, Mechanical, and Solute Properties of MS1700 44

4.4 Model Initial and Boundary Conditions 49

4.5 Summary 54

5 Validation of Model Results **56**

5.1 Validation Methods 57

5.2 Validation Results 58

5.3 Summary 62

6 Results & Discussions **64**

6.1 Introduction 64

6.2 Thermal Model 64

6.3 Mechanical Model 78

6.4 Solute Model 81

7 Conclusion **82**

7.1 Conclusions 82

7.2 Model Limitations & Potential Future Work 83

Appendices **86**

A Material Composition **87**

B Material Property Calculations **88**

List of Figures

1.1 Targets for passenger vehicle fuel efficiency in nine countries [37]. . . 3

1.2 Mild steel (grey) and AHSS grades' (blue, yellow, red) distribution in a typical automotive vehicle [8]. 5

1.3 Elongation-tensile strength diagram for various grades of steel [28]. . 6

1.4 Schematic of a continuous caster, showing the unbending section and labelled faces. 9

2.1 Fe–C phase diagram up to 6.7 wt% Carbon [111]. 13

2.2 Flow phenomena in the continuous casting mould region. This figure has been reproduced from Ref. [80] with permission copyrighted by the Association for Iron & Steel Technology. 16

2.3 Transverse cracks forming across oscillation marks on a steel slab. This figure has been reproduced from Ref. [36] with permission copyrighted by The Iron and Steel Institute of Japan. 21

4.1 Model schematic of Stelco's Lake Erie Works continuous caster. . . . 38

4.2 Thermal Properties of MS1700, (a) Density, (b) Specific Heat, (c) Thermal Conductivity, (d) Fraction Solid. 46

4.3 Mechanical Properties of MS1700, (a) Consistency Index, (b) Strain Rate Sensitivity, (c) Thermal Expansion, (d) Yield Stress. 48
4.4 Illustration of successive zones of heat loss in secondary cooling (1) Contact between the steel and the rolls, (2) Heat loss by convection and radiation, (3) Sprayed Zones. This figured has been modified from Ref. [64] with permission copyrighted by John Wiley and Sons. 51
4.5 Schematic of the water spray nozzle spray pattern. The larger angle, α, and the smaller angle, β, are shown. 52
4.6 Schematic of amount of water spray on the surface of the steel in a Gaussian distribution [1]. 53

5.1 Pyrometer temperature data showing the variation in temperature during casting at the loose side centre at unbending and end of cast for (a) 1005, and (b) 1022. Approximate median temperature lines are labelled. 58
5.2 Effect of the roll cooling on the surface temperature on the loose side broad face and shell thickness evolution. Shown are two examples with roll cooling before (the first number) and after (the second number) unbending. 60
5.3 Comparison of predicted to measured surface temperature measurements for (a) 1005, and (b) 1022. 61
5.4 Comparison of model to measured shell thickness measurements for (a) 1005, and (b) 1022. 62

6.1 Upper: Schematic of predicted shell growth along the narrow face centre. Lower: Predicted evolution of shell thickness along the cast length. 66

6.2 Schematic of predicted evolution of shell thickness along the broad face centre. 67
6.3 Predicted evolution of temperature at the centre, loose side surface, and fixed side surface. 68
6.4 Surface temperature profile along the broad face unbending region on the (a) Loose Side and (b) Fixed Side. The black lines indicate the position of the rolls. 70
6.5 Surface temperature profile within the ductile temperature region along the unbending region on the narrow face. The black lines indicate the position of the rolls. 71
6.6 Surface temperature profile within the ductile temperature region along the unbending region on the (a) Loose Side and (b) Fixed Side. The black lines indicate the position of the rolls. 73
6.7 Surface temperature profile along the unbending region on the loose side broad face with conditions of (a) 60% baseline water spray and (b) 1.05 m/min casting speed. 76
6.8 Main effects plot of casting speed and amount of water spray on the area of the broad face that is within the ductile trough temperature region. 77
6.9 Surface temperature profile during unbending along the (a) Loose Side and (b) Fixed Side. The black lines indicate the position of the rolls. 79
6.10 Von Mises stress during unbending on the (a) Loose Side and (b) Fixed Side. The black lines indicate the position of the rolls. 80

6.11 Segregation profile of manganese on the narrow face centre along the cast length. 81

List of Tables

1.1 Composition of MS1700 (wt.%). 7

4.1 Solute Properties of MS1700 49

6.1 Analysis of the effect of casting speed and spray cooling on the area of the unbending region that is within the ductility trough (738–805℃) on the fixed side, loose side and narrow face. 75

A.1 Composition of 40cmd8 (wt.%). 87

Notation, Definitions, and Abbreviations

Notation

$\alpha(\mathbf{T})$	Coefficient of Thermal Expansion
α	Shimada heat transfer coefficient
β^e_ω	Solute dilation coefficient
β_T	Thermal dilation coefficient
C_p	Specific heat capacity
C_V	Casting speed
D^e_{liq}	Coefficient of chemical diffusion
$\dot{\epsilon}$	Strain rate tensor
E	Fourth order tensor of elasticity
ϵ_r	Emissivity
E_Y	Young's Modulus
f_c	Shimada calibration factor
f_{liq}	Volume fraction of liquid

f_{sol}	Volume fraction of solid
h	Heat Transfer Coefficient
h_{cv}	Convection heat transfer coefficient
k	Thermal conductivity
$K(T)$	Consistency of material
L	Latent heat of transformation
$m(T)$	Sensitivity of flow stress to strain rate
M_{liq}	Slope of the liquidus
n	Normal vector exterior to sub-domain
$\mathbf{n(T)}$	Strain Hardening Exponent
Ω	Sub-domain
ω_{liq}^{e}	Solute concentration of chemical element in liquid
ρ_{ini}	Initial density
$\dot{Q}$	Heat Source Term
R_{ij}	Contact thermal resistance
σ	Stefan-Boltzmann constant
σ_c	Cauchy stress tensor
σ_s	Plasticity threshold
T	Temperature
t	Time
T_0	Reference Temperature
T_j^S	Surface temperature of adjacent sub-domain
T_{ext}	Exterior temperature
θ	Angle of slab with respect to horizontal

T_W	Water temperature of spray
ν	Poisson's ratio
V_S	Mass flux of water in sprays
ω^e_{ini}	Initial concentration

Abbreviations

AHSSs	Advanced High Strength Steels
BCC	Body-Centered Cubic
CAFE	Corporate Average Fuel Economy
CP	Complex-Phase
DP	Dual-Phase
EVP	Elasto-viscoplastic
FCC	Face-Centered Cubic
FEM	Finite Element Method
HF	Hot-Formed
HSLA	High Strength Low Alloy
HTC	Heat Transfer Coefficient
MS	Martensitic
TRIP	Transformation-Induced Plasticity
TWIP	Twinning-Induced Plasticity

Chapter 1

Introduction

This chapter gives an overview of Advanced High Strength Steels (AHSSs), discussing their background, classification, advantages over other grades, and the challenges associated with the manufacturing process. Next, an introduction to the continuous casting process is given. The chapter concludes by outlining the main goals of this work and the chapters of this thesis.

1.1 Overview

Steel is a vital part of the industrial world with a wide variety of applications. 1.88 billion tons of steel was manufactured in 2021. Its properties and relative ease of manufacturing make it ideal for many uses. AHSSs are a class of steels primarily used for automotive applications. In particular, an AHSS grade known as MS1700 is the focus of this work. Steel's foremost manufacturing method, continuous casting, comprised 96% of steel made in 2021 [7]. This method allows for high quality steel created with high output. However, during casting, defects will occur. MS1700

experiences some casting defects, such as cracking and macrosegregation, which can be observed in the cross-section after casting [15]. There are various on-line measurement tools, which include thermocouples and pyrometers to measure surface temperature. These tools are very costly and degrade quickly due to the high temperature (500–1550℃) process. Additionally, industrial trials are generally time-consuming and expensive. Due to this, the construction of a computer model is a very appealing solution. By creating a computer simulation, it subverts this cost, as well as allows the investigation of different casting parameters. It is a considerable challenge to apply an FEM model to solve realistic problems, since many important phenomena such as constitutive equations, thermal-mechanical coupling, contact, and three-dimensional complexities must be taken into account [44]. By using a commercial FEM package which is already capable of handling many of these difficult problems as well as other features such as rich element libraries, advanced computational algorithms, and embedded pre- and post-processing capabilities, the implementation and creation of a model can be focused on [44]. There are various software that can be used to create a continuous casting model, such as Procast, THERCAST and Abaqus, which have been used successfully in the past [12, 36, 43, 105]. For this work, the THERCAST software package is used due to its rich material property database, advanced computational algorithms, and diverse computational options.

1.2 Background of AHSSs

Steel has a wide variety of applications such as automotive vehicles, planes, skyscrapers, and rails due to its high strength, good machinability, and ease of manufacturing [9]. Due to this, new compositions and manufacturing techniques are continuously

being developed, with the goal of creating a lighter material with equal or greater mechanical properties. This is particularly a driving force in the automotive industry due to their need to meet the Corporate Average Fuel Economy (CAFE) standards which are imposed to improve transportation efficiency and reduce global warming emissions [37]. Figure 1.1 shows the increasing historical performance of passenger car fuel economy, as well as future targets. For Canada, the target mileage is 55 miles per gallon in the year 2025. To meet these targets, lighter and stronger materials must be used. Although other materials such as Al and Mg can alternatively be used for this purpose, the lower cost and ease of manufacturing makes steel a more attractive option.

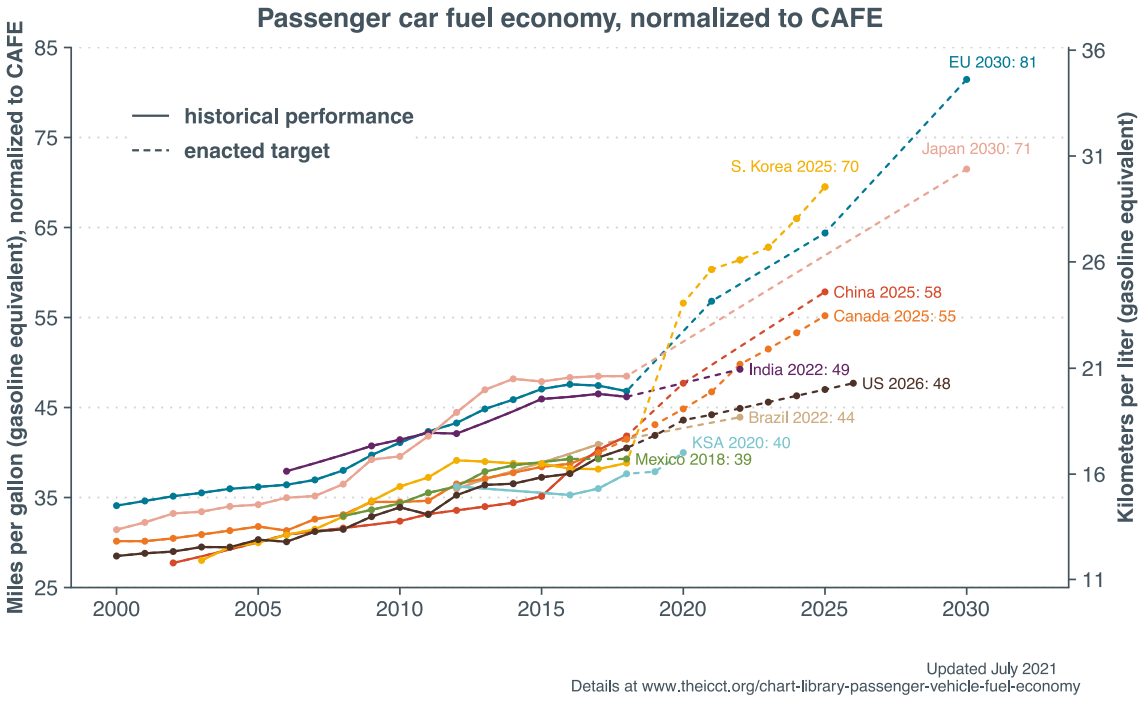

Figure 1.1: Targets for passenger vehicle fuel efficiency in nine countries [37].

1.2.1 Advantages of AHSSs

AHSS grades of steel have significant advantages over conventional steels for automotive applications. They are multiphase steels with complex microstructures that contain phases including ferrite, martensite, bainite, and austenite [69]. Due to this, they have high yield strengths and high work hardening rates, but are lighter than other conventional steels. The strength properties of AHSSs have been approximately defined as a yield strength of $\geq$300 MPa, a tensile strength of $\geq$600 MPa [49], and an elongation between 20-30% [40]. AHSSs also have excellent energy absorbing properties and high fatigue resistance [75]. The use of AHSSs over traditional grades of steel can reduce a vehicle's structural weight by up to 25% and can diminish total life cycle CO2 emission by up to 15% [2]. In addition, these properties make AHSSs widely used in automobiles, comprising as much as 60% of the body structure [55]. Due to these advantages, the global AHSSs market is expected to grow from USD 24.14 billion in 2021 to USD 36.49 billion by 2028 [56].

1.2.2 Classification of AHSSs

There are approximately 30 steel grades that are used presently in the automotive industry [19]. Their purpose and position in an automobile is determined by their mechanical properties. The distribution of mild steel (grey) and AHSS grades (blue, yellow, red) in a vehicle is shown in Figure 1.2. Conventional steels such as mild steel with a low tensile strength of 400 MPa are commonly used in the body structure and the trunk due to their ductility and formability [69]. Recent vehicles have begun to replace the mild steel with thin gauges of AHSSs to further reduce weight [72, 94].

Figure 1.2: Mild steel (grey) and AHSS grades' (blue, yellow, red) distribution in a typical automotive vehicle [8].

The first generation of AHSSs consisted of primary ferrite-based microstructure and included grades of steel such as Dual-Phase (DP), Complex-Phase (CP), Martensitic (MS), and Transformation-Induced Plasticity (TRIP). The first generation of AHSSs had more formability than previous steels, while matching their strength [69]. This is due to its multiphase microstructure, creating a balance between formability and strength.

The second generation of AHSSs was developed based on an austenitic microstructure and includes Hot-Formed (HF), and Twinning-Induced Plasticity (TWIP) grades. This generation improved on the limited formability of the first generation, however, this came at the cost of alloying elements, leading to significantly higher cost [9]. Additionally, they suffered from complex manufacturing processes, which lead to defects. For example, TWIP steel which contains high Mn is prone to delayed cracking as well as embrittlement [41]. Other issues include poor castability, difficult hot working conditions, and poor corrosion resistance [31].

The third generation of AHSSs, which is currently being developed, aims to improve on the formability of the first generation while maintaining cost-effectiveness [95], aiming for properties in between the first and second generations. These steels typically have retained austenite in a bainite or martensite matrix, as well as ferrite or precipitates to create these properties [95].

Shown in Figure 1.3 is the elongation-tensile strength diagram for AHSS first, second, and third generation steels, as well as other grades. It shows the mechanical property advantage of the second generation, as well as the goal mechanical properties for the third generation.

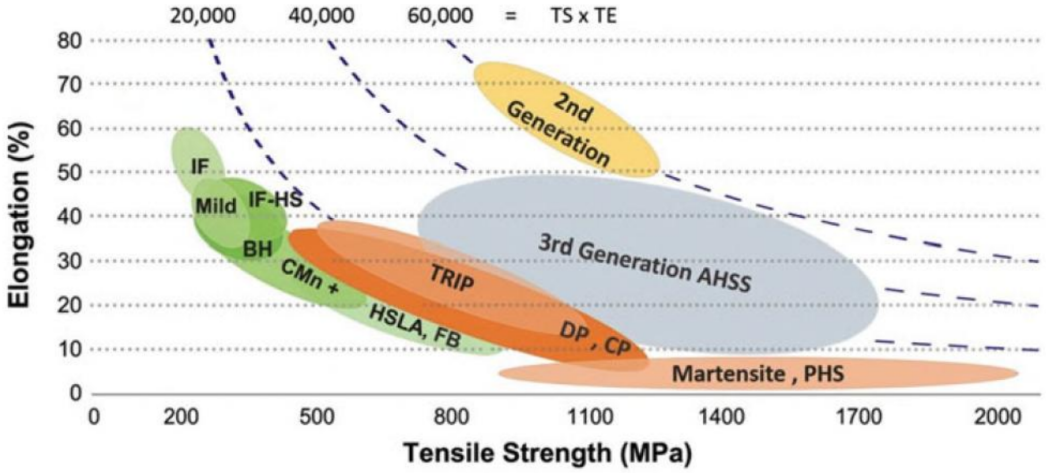

Figure 1.3: Elongation-tensile strength diagram for various grades of steel [28].

1.2.3 MS1700

MS1700 is the alloy that is the focus for this work. It is an AHSS MS grade steel that is lightweight but still has excellent mechanical properties. Its main application is as an automotive steel for safety parts for shock resistance [6]. Its composition is shown in Table 1.1. Its primary alloying elements are Mn, Si, and Cr, in addition to

other elements added in lesser quantities.

Table 1.1: Composition of MS1700 (wt.%).

C	Mn	P+S	Si	Cu+Ni	Cr	Ti	B	Al	Fe
0.25–0.35	1.00–1.50	<0.025	0.50–1.00	0.20–0.40	0.30–0.60	0.040	0.002	0.035	Balance

1.3 Overview of Casting Process

The continuous casting process was patented in 1865 [71], and has undergone many improvements since then to become the high yield, high quality, and cost-effective process it is today. First, molten steel from a ladle flows into the tundish to act as a buffer, and then through the submerged entry nozzle into the mould, which oscillates to prevent the solidifying steel from sticking to the mould wall [80]. As the steel moves through the caster, the molten metal is continuously fed into the mould to maintain an even meniscus level. An oxide mix powder [14], also known as flux powder, is used to cover the exposed liquid steel surface of the mould to prevent oxidation [3]. The mould is cooled, causing rapid heat extraction of 30% of the total sensible heat [35] from the liquid steel, called primary cooling. Due to steel shrinkage upon cooling, moulds are tapered to facilitate heat extraction [24]. After the steel exits the mould, the weight of the steel, known as ferrostatic pressure, is supported by the steel shell and the motor-driven rolls. These rolls also drive the steel through the caster. Between the support rolls, there are high-pressure nozzles used to spray water onto the steel surface to extract heat during casting, known as secondary cooling. The secondary cooling occurs on both wide faces of the steel (the broad face). However, the loose side (inside radius broad face of the steel) and the fixed side (outside radius

broad face of the steel) may have different amounts of cooling. Additionally, there is no direct cooling on the narrow face (the steel short face) following the exit from the mould.

The steel begins casting vertically, and it is transitioned into a horizontal direction over a length of about 10 m during casting [3], called the bending and unbending section. Each caster has a unique geometry, and some, like that of Stelco Lake Erie Works, only has an unbending section. This section is indicated by a change in radius at the start and the end. This, in addition to the labelled fixed and loose side faces, is shown in Figure 1.4. Once the steel is fully solidified, it is then torch cut at the appropriate length and transported to the next step in the process.

As-cast steel products come in various shapes, such as billets (square cross-sections with thickness less than 170 mm), thick slabs (wide rectangular cross-section with thickness between 180 and 300 mm), thin slabs (thickness between 50 and 75 mm), strips (thickness between 1 and 12 mm) [27], and beam blanks (large dog-bone-like sections that are directly fed into an I-beam or H-beam rolling mill, ranging from 250 to 1150 mm wide) [17].

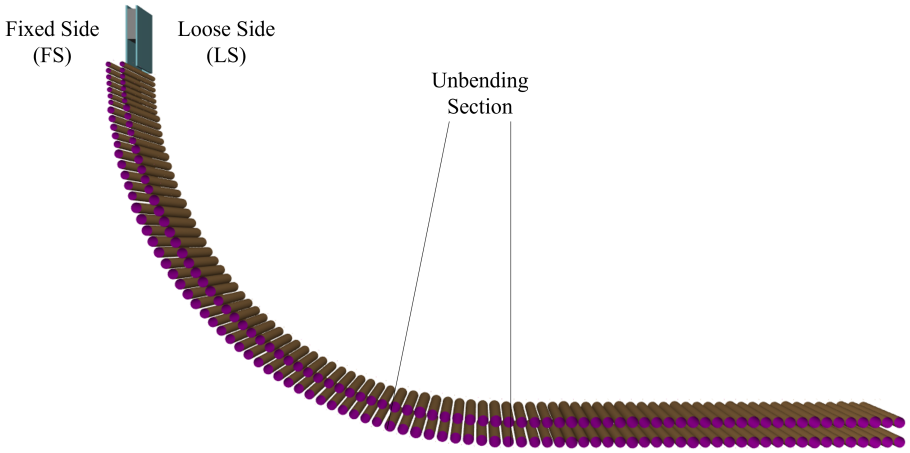

Figure 1.4: Schematic of a continuous caster, showing the unbending section and labelled faces.

1.4 Outline

This thesis proposes the use of a thermo-mechanical-solute physical model to investigate the formation of defects during the continuous casting process of steel.

This thesis is organized in the following order:

Chapter 2 describes the principles of thermal, mechanical, and solute simulation, and provides a review of basic knowledge, relevant experimental investigations, and noteworthy continuous casting simulations.

Chapter 3 presents the scope and objectives of this thesis. This includes a short review of the gaps in previous models and key improvements.

Chapter 4 presents the methodologies used in this thesis. This includes the model assumptions, equations, material properties, as well as initial and boundary conditions.

Chapter 5 outlines the model validation with experimental measurements. The results of the validation are presented and discussed.

Chapter 6 reports the applications of the model to various conditions and the corresponding results.

Chapter 7 summarizes all contributions of this thesis, concludes with model limitations, and provides suggestions for future work.

Chapter 2

Literature Review

2.1 Introduction

In this chapter, in Section 2.2, the solidification of the Fe-C system is described, including the phases present during the steel continuous casting process, and the effect of the carbon content on the mechanical properties. Next, in Section 2.3, the typical defects present in the continuous casting process, such as transverse cracking and macrosegregation, are described, as well as experimental approaches present in literature. Subsequently, in Section 2.4, the thermal, mechanical, and solute simulation approaches in literature are summarized. Lastly, prior models in literature are reviewed and gaps are identified.

Research into the mathematical modelling of the continuous casting process can be separated into three types of finite element models: Thermal models that predict the evolution of temperature and fraction solid during casting, thermal-mechanical models that, in addition to the temperature, predict the strain and deformation during casting, and thermal-mechanical-solute models that also include alloy

segregation. This final class is rare due to the many complex phenomena that must be taken into account.

2.2 Solidification

Solidification is a phase transformation process in which a liquid turns into a solid. For a pure metal, solidification occurs when the temperature reaches the melting point. For alloys such as steel, solidification occurs over a temperature range and can involve the formation of one or more solid phases [26].

Steel Phases

Shown in Figure 2.1 is the Fe-C phase diagram. A mixture of iron and carbon is considered steel up to around 2.5 wt% carbon, however commercial steels usually range from 0.005 to 1.0% [22]. Steel solidifies from liquid at approximately 1538℃ (depending on the alloying elements) into a body-centered cubic (BCC) structure known as δ-ferrite [22]. Ferrite is a solid solution of carbon in iron that is strong and ductile, and a common component in steel. Upon further cooling, at 1395℃, δ transforms into a face-centered cubic (FCC) lattice known as austenite, or γ-iron [22]. It is a high strength, ductile, high temperature phase. As cooling proceeds, at 910℃, the lattice structure returns to body-centered cubic as ferrite again, known as α-ferrite [22]. Indicated as well on the phase diagram is that steel greater than 0.8 wt% C which undergoes eutectoid transformation, and those less than that which do not.

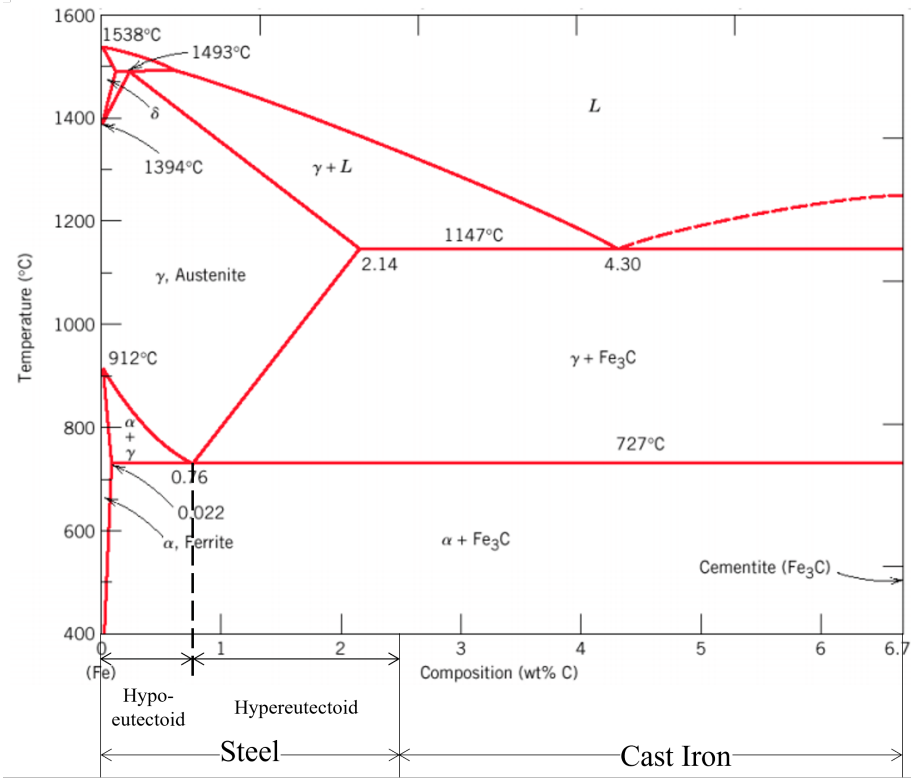

Figure 2.1: Fe–C phase diagram up to 6.7 wt% Carbon [111].

Mushy Zone

A pure element solidifies from a liquid into a solid immediately. However, in an alloy, the additional elements cause the solid and liquid phases to exist over a range of temperatures. The temperature range between the solidus (when the material is completely solid) and liquidus (when the material is completely liquid) temperatures is known as the mushy zone. As can be seen on the Fe-C phase diagram in Figure 2.1, the mushy zone is between the liquid and the solid regions, where the liquid and solid exist simultaneously.

2.3 Defects in Continuous Casting

From the tundish to the end of the caster, there are many possible causes of defects throughout the continuous casting process. These defects range from surface defects that can be detected and subsequently removed through scarfing (oxyacetylene torch removal), to severe defects such as shell thinning, which can lead to the failure of the steel shell. Although much progress has been made since the inception of continuous casting to minimize these defects, they continue to plague steelmakers worldwide.

2.3.1 Mould Defects

Solidification during the continuous casting process involves many complex inter-related phenomena. Shown in Figure 2.2 is the flow phenomena in the continuous casting mould region, illustrating some causes of defects in the mould. In the mould, the molten steel is transported at the desired flow rate into the mould cavity through the submerged entry nozzle. This steel must be at the correct temperature without excessive turbulence, and the flow conditions must minimize exposure to air, avoid entrainment of slag and other foreign material, promote the removal of inclusions, as well as encourage uniform solidification [80]. To allow for the movement of the steel shell along the mould, when flux powder melts it goes between the solidified steel shell and the mould, acting as a lubricant. However, this lubricant alone is not sufficient for the shell to move down the mould, so the copper mould undergoes periodic vertical oscillation. A side effect of this is a groove perpendicular to the casting direction on the surface of the steel, known as an 'oscillation mark', typically 0.1-1 mm deep [24]. Oscillation marks can also act as a stress concentration point to initiate cracks and

also trap inclusions which can lead to serious defects.

Due to the complex flow process, many quality problems in the mould can be directly attributed to poor control of fluid flow conditions. For instance, molten steel jets directed by the submerged entry nozzle can hit the narrow faces, causing shell thinning, which at the extreme leads to a complete failure of the shell, known as a breakout [80]. The jets also carry bubbles and inclusion particles into the mould. If the flow pattern is such that they reach the meniscus of the liquid steel, they can be captured into the liquid slag layer. However, an improper flow pattern will carry the bubbles and inclusions into the molten steel or entrap them into the solidifying steel shell, causing surface defects. If these are not removed, then they will lead to line defects or slivers in the final products [57, 80]. The momentum of the upward flowing jets has a significant effect on the casting quality as well. If it is too high, then it can raise the meniscus level, causing a nonlinear profile along the top surface. Excessive turbulence in this manner can disrupt stable solidification, leading to deep oscillation marks, surface depressions, surface cracks, and local entrapment of mould slag [16, 80]. Deeper oscillation marks can in turn lead to cracks during secondary cooling.

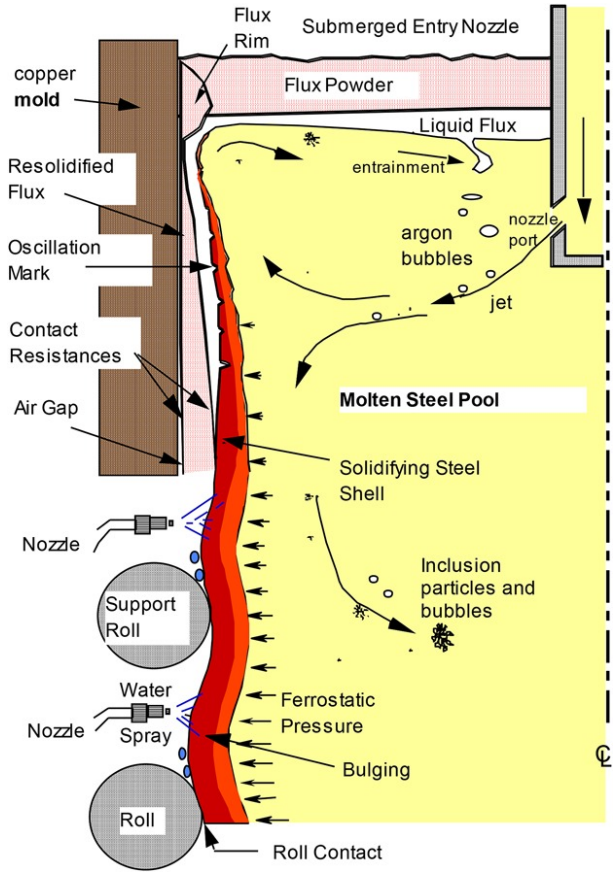

Figure 2.2: Flow phenomena in the continuous casting mould region. This figure has been reproduced from Ref. [80] with permission copyrighted by the Association for Iron & Steel Technology.

Hot-Tear Crack

A hot-tear crack is a defect that is formed during solidification of the steel strand starting at the meniscus and mould walls [36] caused by a combination of tensile stress and metallurgical embrittlement [81]. These cracks form in the mushy zone, near the solidus temperature, and embrittlement is so severe near this temperature that hot-tear cracks can form at strains on the order of only 1% [81]. Hot-tear cracks form due to thin liquid films between the dendrites at grain boundaries being susceptible

to strain concentration, such as by irregular solidification [36]. This leads to the separation of the dendrites and intergranular cracks [81]. Hot-tear cracks that form in the mould wall are subjected to thermal strain as well as mechanical strains from roll pressure, ferrostatic pressure, machine misalignment, and bending and straightening, resulting in the propagation of the crack [27].

2.3.2 Transverse Cracking

A transverse crack occurs at the steel surface, transverse to the casting direction. If this crack is on the narrow face, it is known as a transverse edge crack. Transverse cracks that occur after the mould, in the secondary cooling zone, form within the low ductility regions of steel [77, 99].

Low Ductility Region

The low ductility region, or ductility trough, of steel is a temperature region of low ductility that occurs between 600–1500℃, although the most common region is between 600–900℃ [77]. It is defined as the region where the reduction in area during fracture is lower than 40% [89]. Within this range, the steel strand is much more susceptible to brittle fracture, which can lead to cracking. The steel composition affects the low ductility region, so its effect on the process can vary [76, 89].

Temperature Range

A hot ductility embrittlement types are described as [18]:

- Type I: Embrittlement by incipient melting
- Type IIa: Embrittlement by second phase particles–(Mn, Fe)S

- Type IIb: Embrittlement by second phase particles–Nb(CN), AIN, V(CN)
- Type III: Embrittlement by transformation

Type I

Occurs at high temperature, typically 20–50℃ below the mean solidus temperature. It is caused by incipient melting at interdendritic and grain boundaries, and can be characterised by inter-dendritic failure and the presence of particles such as MnS [18, 77]. This type of ductility trough may be the cause of the initiation of transverse cracks in the mould [77].

Type II

Occurs over a temperature range of 900–1200℃. The fracture surface typically is found along austenite grain boundaries, and can show the presence of second phase particles [18, 77]. These types are associated with particles such as (Mn, Fe)S for type IIa and Nb(CN), V(CN), Ti(CN) and AIN for type IIb [18, 77].

Ductility loss in type IIa has been associated with precipitation of liquid FeS particles and the reduction of grain boundaries de-cohesion due to sulphur segregation. By contrast, type IIb has been linked to the presence of carbon nitrides causing austenite grain boundary sliding, leading to crack formation at grain boundaries [77]. Type IIa and IIb are further contrasted by the effect of strain rate. Type IIa's ductility drop is only apparent at high strain rates, whereas type IIb's ductility loss decreases as strain rate increases [18, 77].

Type III

Occurs over a temperature range of 600–900℃. If the Type II region is present, then these two regions can intersect and exist simultaneously. Type III fracture surfaces are characterised by intergranular failure, and the facets of the individual grains are commonly associated with void formation around the second phase particles [18, 77]. Steels which undergo hypoeutectoid transformation, such as MS1700, are associated with this region [76].

The ductility loss in this region is associated with the formation of proeutectoid ferrite. During the transformation of austenite into ferrite and cementite, the ferrite will begin forming before the eutectoid transformation occurs. This 'proeutectoid' ferrite will often begin forming at the austenite grain boundaries, especially during casting when the grains are large and precipitates have formed on the grain boundaries [20, 99]. The weaker ferrite phase deforms more easily than the austenite phase, leading to inelastic strain accumulating in the ferrite [96]. This strain accumulates, leading to void formation, coalescence, and eventually failure of the steel along the austenite grain boundary [76]. After the proeutectoid ferrite forms, it will not transform into pearlite, bainite, or martensite as the remaining austenite does. If it had formed on grain boundaries, then the ferrite structure may persist, leading to fracture near the eutectoid temperature [76]. Hypoeutectoid grades such as the focus for this work are especially susceptible to transverse cracking due to the proeutectoid ferrite transformation beginning at higher temperature [76]. The low ductility region for AHSSs is between the Ar3 (starting temperature for transformation of austenite into ferrite during cooling [107]) and Ac3 (the final temperature at which ferrite is completely transformed into austenite) temperatures [109].

Formation of Transverse Cracking

Transverse cracking forms due to longitudinal forces on the strand surface. These forces are due to several phenomena, such as mechanical loading from the drive rolls, friction, bending and unbending from the support rolls, roll misalignment, and thermal strains. The typical formation mechanisms of transverse cracking are as follows:

- **Oscillation marks**: The grooves on the surface of the steel act as a stress concentrator. Oscillation mark depths of greater than 0.3 mm were reported to promote transverse corner cracking, and the severity of the cracking increases with increasing oscillation mark depth [3, 90]. It has been shown that transverse cracks are intergranular and follow the boundaries of large prior-austenite grains (greater than 1 mm in diameter) [20] within oscillation marks and other surface depressions [20, 64, 89, 100, 107]. Additionally, thermal cycling can cause fatigue-induced cracks at bending and unbending regions [76]. An image of transverse cracks occurring along the oscillation marks on a steel slab is shown in Figure 2.3.

- **Inadequate lubrication between the mould and shell**: If there is uneven inflow of mould flux into the mould, a frictional force can occur, causing cracks at the roots of oscillation marks [90].

- **Solute segregation inside the mould**: mould oscillation causes solute-enriched liquid to accumulate at the root of an oscillation mark, which in turn causes the solidified shell to be more susceptible to fracture. If tensile stress is applied to this point, a transverse crack may occur [32].

- **Secondary cooling**: In the spray cooling zone, transverse cracking most commonly occurs at the bending and unbending region due to stress concentration and loss of hot ductility. The low temperature ductility region for AHSSs occurs at a temperature range of 600-900℃, during the formation of austenite [61, 64]. This is the cause of the majority of transverse cracks [76, 89, 99].

- **Other factors**: Other potential causes include caster misalignment, worn support rolls, and strand bulging [90].

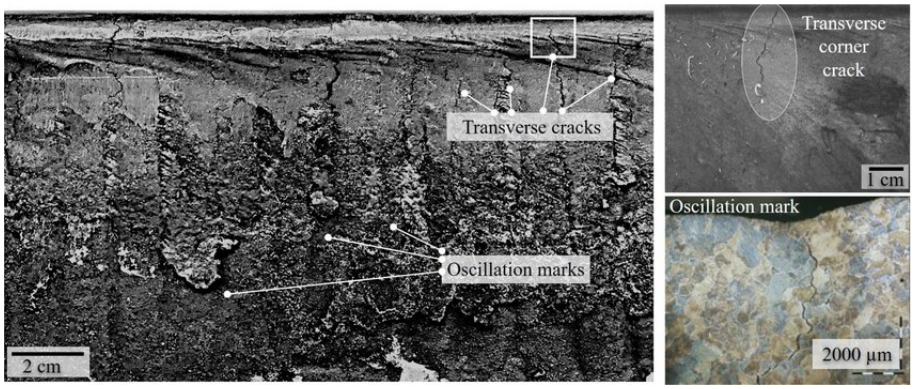

Figure 2.3: Transverse cracks forming across oscillation marks on a steel slab. This figure has been reproduced from Ref. [36] with permission copyrighted by The Iron and Steel Institute of Japan.

Surface defects such as transverse cracking are very detrimental to the productivity of the continuous casting process because they must be removed by a labour-intensive technique such as scarfing or other means before further processing [76]. If the cracks are not successfully removed, then during the subsequent rolling process, they will likely result in surface defects in the final steel product [90].

Previous Studies of Transverse Cracking

To reduce transverse cracking defects, unbending should be carried out outside the Ar3–Ac3 temperature range [90, 99]. However, simply reducing the water spray may affect the length of centreline solidification (metallurgical length), worsen centreline segregation, and reduce the life expectancy of the caster rolls [89]. Previous studies have been successful in using 2D and 3D models to predict surface temperature and subsequently reduce transverse cracking by optimizing the water spray in the secondary cooling zone [36, 76, 89, 90, 99]. Wang *et al.* [89] found that after water spray optimization, there was a large reduction in observed number and size of transverse cracks. No cracks at the slab corner on the inner radius broad face (loose side) were detected, and the crack density on the outer radius broad face (fixed side) decreased from 73.7 to 51 #/m. On the fixed side, the percentage of cracks less than 5 mm in length increased from 71.3 to 83.8%, and the percentage of crack length more than 5 mm decreased. Yang *et al.* [99] implemented a 25% total reduction in water cooling, greatly reducing the amount and size of surface cracks.

It has been found that the greater the slab width, the fewer edge cracks are present due to the slab edge receiving less cooling and thus being outside the ductility trough region [39]. It has also been shown that the mould taper and oscillation marks have a significant effect on the observed transverse cracking, and optimizing these parameters can reduce the defect [39, 89, 107].

2.3.3 Segregation

Segregation is the non-homogeneous partitioning of alloying elements during solidification. It is caused by alloying elements in steel having a higher solubility in the

liquid than in the solid, thus upon phase transformation the solute elements are rejected by the solid into the liquid. This results in the liquid ahead of the solidification front becoming enriched in solute elements [25, 73]. If this is restricted to the solidification front, then only microsegregation is the result. However, bulk scale events such as solidification shrinkage and strand deformations will apply pressure to the mushy zone, causing solute-rich liquid to be forced away from the interface, resulting in macrosegregation as well [73].

Microsegregation

Microsegregation is the non-homogeneous repartitioning of solutes within the dendritic solidification structure, of the order of 10–100 µm [73]. It is caused by dissolved alloying elements being rejected from the solid into the liquid, causing it to be trapped between the arms of the growing dendrites [73]. Microsegregation is not a major quality problem, since the effects can be removed by heat treatment [23, 30].

Macrosegregation

Macrosegregation, also called centreline segregation, is the non-homogeneous repartitioning of solutes across the scale of the whole product. It is the result of slow interdendritic flow of solute-enriched liquid through the mushy zone, which contains solidifying dendrites, and the transport of solid grains or grain fragments throughout the liquid pool [27, 48]. It is unavoidable and is one of the most serious defects in continuous-cast steel, because if present, it cannot be removed by heat treatment due to the large length scales and always impacts the final product [30, 81, 82].

Macrosegregation can cause many problems with the quality of the finished

product, as final products with severe macrosegregation have non-uniform mechanical properties, as well as being more likely to contain subsurface cracks and porosity, and thus must be sold at a reduced cost [30]. It can also be the initiation site for cracking and porosity [30].

The main factors that affect segregation are the steel chemistry, superheat, casting speed, cooling regime, and machine geometry [73]. Various techniques have been used to reduce the degree of segregation, such as electromagnetic stirring, soft reduction (reducing the distance between the fixed and loose side rolls), and optimized process parameters such as casting speed, machine taper, and superheat [73], but none have been successful in completely eliminating it.

2.4 Modelling

2.4.1 Thermal

To simulate the continuous casting process, it is first required that the heat transfer equations are determined. Models to predict temperature distribution and growth of the solidifying shell are a crucial building block for many advanced computational models to couple heat transport with other phenomena [82]. The continuous casting process contains many inter-dependent thermal, fluid flow, solidification, and mechanical phenomena, which makes it exceedingly computationally expensive to model, so assumptions are made for computational efficiency.

A difficult task when developing a solidification heat-transfer model of continuous casting is to accurately model heat removal from the strand surface [82]. This is especially difficult in the mould, where heat transfer is governed mainly by heat

conduction across the interfacial gap between the shell and the mould wall [82]. Heat transfer below the mould also presents difficulties due to complex phenomena such as droplet impingement and film boiling that occur at the strand surface during spray cooling and from roll contact [82]. The most popular approach to these problems is to calibrate the model to match plant measurements, which has proven very effective [50, 53, 63, 66, 68, 98, 105]. Calibration of solidification heat-transfer models in the mould can utilize measurements such as cooling-water heatup for a global energy balance, thermocouple temperatures in the mould walls for a heat-flux profile, and shell thickness measurements from breakout shells or composition profiles after trace-metal injection [50, 53, 59, 68, 74, 79, 88]

Compared to primary cooling models, it is more difficult to validate models below the mould with plant data. Surface temperature can be measured with pyrometers, however, the readings are lowered by steam and surface oxide scale formation. Shell thickness typically involves indirect observations such as tracer injection [50], roll movement [67], internal hot-tears induced by inserting shims between the strand and the rolls [74], the melted tips of nails shot into the strand [52], or the serious defect of whale formation, which occurs when the metallurgical length exceeds the supported length of the strand [66, 67]. Once a validated model has been created, a solidification heat-transfer model is a very powerful tool and a crucial first step to creating a multiphysics model.

Previous Thermal Models

Many techniques and assumptions have been used in literature to simplify the heat transfer equation to apply it to modelling, such as assuming a steady-state system

or using a 1D or 2D model. Prior to the more advanced computer models that exist today, numerical models were developed such as the one by Tiedje *et al.* [83] in 1993, who created a simple 1D model for the mould and strand. Since then, more complex models that take advantage of increased computational power have been created. In 2006, Meng *et al.* [60] created a 1D thermal model to predict the heat transfer and solidification in the mould. To account for the heat conduction in the solidifying steel shell, the 1D transient heat flow equation was applied with temperature-dependent conductivity, neglecting axial heat conduction. This was coupled with a 2D steady-state heat conduction equation in the mould wall. In 2009, Malinowski *et al.* [54] created a 3D FEM model of heat transfer and fluid flow in the mould, using it to study the model response to thermal resistance of the mould-steel interface and the casting speed. An empirical equation was derived to solve the heat transfer problem through the steel-mould interface. The results showed good agreement with the model, and it was used to predict the effect of the thermal resistance of the steel-mould interface, casting speed, and water spray cooling. The predictions were consistent with results published in literature. However, the description of the boundary equations has possibilities for improvement. Thermal models have successfully been used, such as by Zhang *et al.* [107] and Yang *et al.* [99] to predict the temperature to investigate transverse cracking. However, due to increased available computational power, thermal-only models are uncommon in recent literature, as many models focus on coupled thermal-mechanical phenomena.

2.4.2 Thermal-Mechanical

A thermal-mechanical model is required to investigate the distribution and evolution of many important continuous casting phenomena, such as temperature, stress, and strain, which are vital to understand crack formation and segregation [82]. First, a thermal-mechanical model solves the heat transfer equation to determine the thermal state of the material. Next, it must solve the equilibrium equations that relate force and stress, including the constitutive equations that relate stress and strain, and take into account compatibility equations that relate strain and displacement [82]. When solving the mechanical equations, the total strain is divided into thermal, elastic, and inelastic components, the latter of which is required to treat plasticity and creep in the solidifying steel [82]. An accurate computational model must be verified with known analytical solutions such as that of Weiner *et al.* [91], and compared to plant measurements [82]. It is much less common in literature than a thermal model to have a properly verified and validated thermal-mechanical model [82]. Comparison of thermal-mechanical model predictions with stress measurements is rare. Some models have successfully matched lab measurements of temperature and force evolution in solidifying steel specimens [91, 106]. Direct plant measurements of stress during continuous casting are more difficult due to the high temperature process.

Constitutive Modelling

When creating a thermal-mechanical model of the continuous casting process, it is critical to characterize the change in mechanical behaviour of steel as a function of temperature. For this reason, constitutive equations that describe the relationship between temperature, strain rate, stress, and strain are necessary. It is difficult to

perfectly account for the constitutive behaviour, however, partly due to the difficulty of finding accurate experimental measurements of thermal-mechanical properties at the high temperature, low strains, and low strain rates relevant to the casting process [82]. Multiple constitutive approaches have been used, including:

- **Elastic**: Only considers elastic deformation during continuous casting [84].
- **Elastic-perfect-plastic**: Initially linearly elastic and becomes plastic once the yield stress is reached [10, 103].
- **Viscoplastic**: A strain rate-independent plastic behaviour that incorporates strain rate-dependent creep flow as inelastic strain. Steel becomes purely viscoplastic close to the solidus temperature, when the yield stress and strain hardening are negligible [38, 62, 86, 102, 104].
- **Elastic-viscoplastic**: Behaves as a viscoplastic model while incorporating an elastic effect, and thus can take into account strain hardening [43, 46, 47, 51, 70, 92, 102, 103, 110].

An important early approach for constitutive modelling was proposed in 1963 by Weiner *et al.* [91] who derived an analytical solution for the generation of thermal stresses in a 1D metal solidification process by employing a simple elastic rate-independent plastic constitutive model. A creep law was later added by Kristiansson in 1982 [46] to take into account time-dependent inelastic behaviour at high temperatures.

Due to an increase in computational power, more computationally intensive viscoplastic equations have been used in the recent decades. Inoue *et al.* in 1992 [38],

using a modified version of Perzyna's [65] constitutive equation, described elastic-viscoplastic constitutive behaviour during aluminum direct-chill (DC) casting. In 2011, Paquet *et al.* [62] incorporated rate-independent behaviour by using a viscoplastic model based on overstress in their homogenization model of cast aluminum alloys. Elastic, rate-independent plastic constitutive models are generally sufficient for ambient temperatures for steel [104]. However, at high temperature, steel exhibits time-dependent inelastic behaviour due to bulging effects, and creep must be taken into account as it is significant at these temperatures [4, 51]. Unified viscoplastic constitutive models that treat rate-independent plastic strain and rate-dependent creep together as inelastic strain are very commonly used in modelling of steel casting. In 1982, Anand [5] developed the first model of this kind based on multiple evolving internal state variables, which has been used in many thermal-mechanical models of metal at high temperatures. In 1992, a decade later, Kozlowski *et al.* [45] introduced a simple constitutive equation to model austenite, relating inelastic strain, as a single structure parameter to strain rate, stress, temperature, and steel grade with carbon content. In order to model the body-centred cubic δ-ferrite phase, Zhu in 1996 [110] developed a power law-based constitutive model to account for much higher creep rates of this phase when compared to the face-centred cubic austenite phase. These models have been very popular since they were introduced, and been used in many steel solidification papers [42, 51]. Additionally, previous work has found that elastic-viscoplastic models are excellent for modelling high-temperature inelastic flow behaviour of steel at high temperatures [45]. However, this comes at a greater computational cost.

Previous Thermal-Mechanical Models

Building on previous analytical models, computer-simulated Finite Element Method (FEM) models have been used to analyze the continuous casting process. Simple one-dimensional thermal-only models that only included the mould such as that developed by Meng *et al.* [60] were used initially, but as available computational power grew, so did the complexity of the models.

Building on previous analytical and computational models, a thermal-mechanical FEM model was developed in 2004 by Li *et al.* [51], which simulated a transverse section of the steel strand under the assumption of generalized plane strain, meaning that the strain is independent of thickness [51]. This model can quantify the temperature, stress, and strain distributions in the solidifying shell, and was validated using an analytical solution of thermal stress from Weiner *et al.* [91]. Pascon *et al.* [64], in that same year, developed a 2.5D FEM model that incorporated thermal-mechanical effects to study the formation of transverse cracks during secondary cooling, using a generalized plane strain assumption. To create a 2.5D model, thin 2D perpendicular slices were modelled, and under the generalized plane strain assumption, a three-dimensional view of the strand was formed.

Koric *et al.* [44] in 2007 pioneered the 3D solidification modelling of complex geometry for continuous casting. They developed a 3D thermal-mechanical primary cooling model for shaped sections such as thin slabs, using the generalized plane strain assumption, and validated using the analytical solution from Weiner *et al.* [91]. This model was applied to study the behaviour up to 30 cm below the mould. Koric *et al.* [43] in 2009 expanded on previous work and developed an explicit 3D thermal-mechanical model which incorporated rate-dependent constitutive laws. This model

was used to simulate temperature and stress development in solidifying shell sections in the mould, including the effects of ferrostatic pressure, narrow face taper, and mechanical contact.

Subsequently, there have been numerous 3D thermal-mechanical models developed. Many of these models have used the generalized plane strain assumption [33, 43, 44, 51, 64, 104, 105], and have been used to investigate various phenomena such as mould air gap formation [12, 29, 34], mould taper optimization [34, 51], strand bulging during casting [29, 64], transverse crack formation [33, 34, 36, 64], hot-tear cracking [29, 51], or the temperatures and stress development on the solidifying shell [29, 33, 34, 43, 44, 51, 104, 105]. Models of the full cast length that do not use the generalized plane strain assumption are uncommon [29, 36].

Gaps in Prior Thermal-Mechanical Models

Although there has been significant development of 3D thermal-mechanical models in recent years, there are still some gaps in the current literature. Many models have focused on the mould effects exclusively and not modelling secondary cooling. Others that have taken into secondary cooling have used a generalized plane strain assumption for computational efficiency. Models that have not used a generalized plane strain assumption have exclusively focused on the formation of transverse cracking and not investigated other phenomena. Additionally, there has not been any investigation into the effect of soft reduction on the stress experienced by the strand and its relationship with transverse cracking. Lastly, each caster has a unique geometry, so the results and optimizations will be unique to each caster and grade.

2.4.3 Thermal-Solute

Solute macrosegregation is very difficult to model because it requires an accurate thermal-solidification model, a model of microsegregation between dendrites, macroscale fluid flow that redistributes the solute, volumetric thermal shrinkage, and mechanical deformation which induces the flow, and lastly failure of the microstructure, which accumulates the solute locally into a defect [82]. Many prior segregation models at the local scale between dendrite arms have been developed [82, 93, 101]. However, although significant progress has been made since a decade ago, macrosegregation modelling is still in its early stages [82]. Most models have a thermal-fluids modelling approach, solving mass and momentum transport equations for the fluid, combined with conservation and transport equations for the solute, and include methodologies to handle the transport and removal of latent heat, the phase transformation from liquid to solid, movement of the solid, and a microsegregation model [21, 27, 58, 82, 97, 108]. Some thermal-fluid-solute models focus on centreline segregation to describe bulging between support rolls and mechanical soft reduction [11, 21, 58, 82, 97, 101]. Important effects on solute transport of the columnar and equiaxed microstructure, including local deformation and failure, remain a challenge for macrosegregation models in the mould [82], although one model developed by Zhang *et al.* [108] investigated the effect of mould electromagnetic stirring on the formation of the equiaxed zone, and another meso-scale model by Feng [27] predicted the solidification of equiaxed dendritic growth, hot-tear cracking, and centreline segregation. However, more work is needed on quantitative validation of macrosegregation models [82].

Previous Thermal-Mechanical-Solute Models

Thermal-mechanical models that include segregation are exceedingly rare due to the difficulty in incorporating the different time scales required [81]. In one example, Fachinotti *et al.* [25] created a thermal-mechanical and macrosegregation model that considered a solidifying alloy as a binary mixture of a solid and a liquid phase. The compressible viscoplastic constitutive model used did not take into account strain hardening. The model was used to simulate fluid flow, solute transport, and mechanical deformation of the solidifying shell to predict the bulging of the support rolls and centreline segregation.

2.5 Use of a Model for Industrial Applications

As discussed, there exists many models of the continuous casting process in literature [29, 34, 44, 51, 64, 82, 104]. However, each caster has a unique geometry, and each steel plant has unique practices for every facet of the casting process, such as grade chemistry, mould powder utilization, mould oscillation, casting speed, water cooling, as well as many others. Therefore, it is imperative that models that are intended to be used to optimize the casting process of a specific caster are tuned to the geometry and casting practices of the specific caster. This will create a robust model that can be used to investigate many steel grades and casting practices, thus improving the casting process, and eliminating the expense of casting trials.

Chapter 3

Scope & Objectives

The demand for AHSSs is continuously increasing due to their exceptional combination of mechanical properties and weight reduction. However, they commonly present defects such as cracking and macrosegregation. If these defects are severe, the mechanical properties are reduced and the product must therefore be down-graded, leading to a large loss in profit.

This work was done in collaboration with Stelco Lake Erie Works. They have found that the AHSS grade that is the focus of this work, MS1700, has been presenting transverse cracking and macrosegregation defects that have led to the inability to cast it. To solve these problems, the objective of this MASc project is to develop a 3D thermal-mechanical-solute model of steel solidification using the THERCAST software package to understand the behaviour of Stelco's Lake Erie Works continuous caster. This model will then be applied to the casting of MS1700 to optimize the process parameters to improve the castability of this grade for the continuous casting of slabs. Particularly, the parameters to reduce transverse cracking, which is caused by critical strain within a steel's low ductility temperature region, will be focused on.

Objectives

The objectives of this thesis are as follows. First, to develop a 3D thermal-only model that takes into account heat transfer from the mould, sprays, rolls, and ambient temperature. Second, to optimize the casting speed and spray cooling to reduce transverse cracking. Third, to create a preliminary solute transport and mechanical model of the caster to develop a 3D finite element thermal-mechanical-solute model.

Chapter 4

Methods

4.1 Introduction

In order to investigate defect formation during continuous casting, the thermal, mechanical, and solute information must be known. To create the model, the following is required:

- Calculation domain, geometry, and formulation
- Thermo-physical-solute material properties
- Boundary and initial conditions

In this chapter, a 3D coupled thermal-mechanical-solute solidification model of the continuous casting process is proposed to investigate transverse edge cracking phenomena in collaboration with Stelco Lake Erie Works. In Section 4.2 an overview of the model as well as assumptions used will be given. In Section 4.3, the equations for the material properties used are reviewed. Lastly, in Section 4.4 the initial and boundary conditions used in the model are discussed.

4.2 Model Formulation, Domain, and Geometry

The finite element model was created using THERCAST, as it has been used successfully in the past [12, 29, 36, 81]. It is a 3D finite element commercial software for foundry processes developed by CEMEF (MINES ParisTech) and Transvalor. More detailed information about the algorithms used by the model can found in the THERCAST manual [85].

4.2.1 Model Domain

The analysis domain includes the top of the mould to the end of the caster. The model geometry is a rectangular slice with a cross-section of 2 m by 0.2493 m, and a length of 2 m. By implementing a symmetry plane along the centreline on the narrow face, the problem is reduced to a half-section, with actual dimensions 1 m by 0.2493 m. The casting was modelled until the slice was completely solidified. To simulate the thermo-physical-solute effects, a global non-steady state approach was used with an updated Lagrangian field calculation.

4.2.2 Model Geometry

Stelco's Lake Erie Works' provided the geometry of the caster. The caster geometry, including the 87 support rolls and 254 nozzles, are input into the THERCAST software. Stelco's caster also uses a soft reduction approach to reduce macrosegregation. This approach involves an intentional thickness reduction by reducing the distance between the rolls. The model schematic from THERCAST is shown in Figure 4.1.

Finite Element Mesh

The finite element mesh for the model was constructed using tetrahedral nodes with a constant mesh size of 0.02 m.

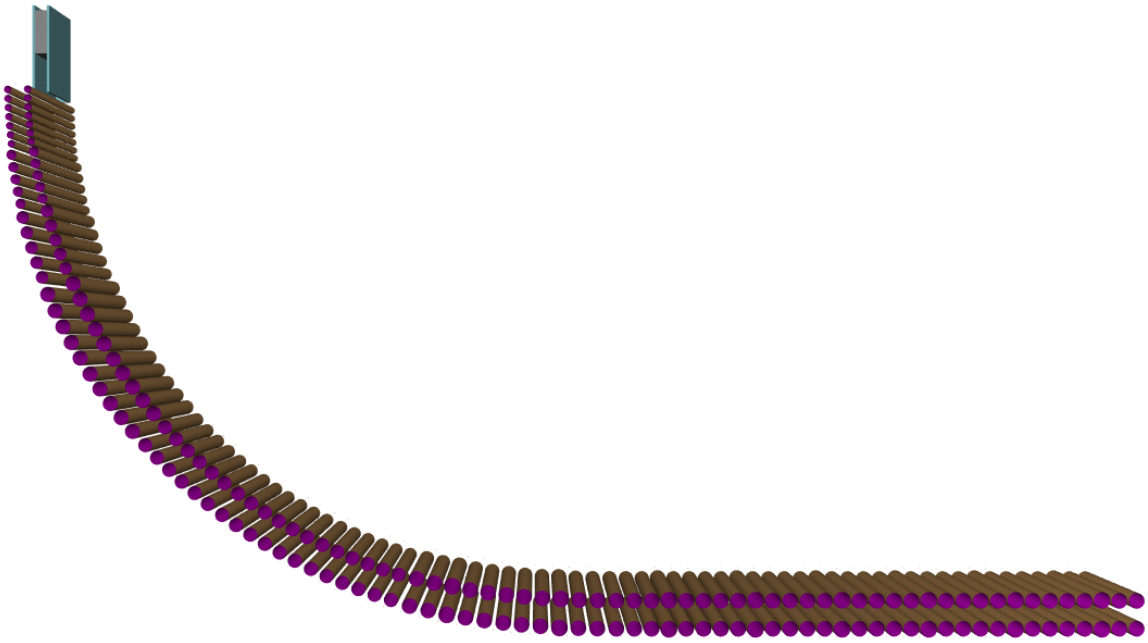

Figure 4.1: Model schematic of Stelco's Lake Erie Works continuous caster.

4.2.3 Analysis Formulation

The THERCAST model first requires the solution of the heat transfer analysis. Next, the solute movement is calculated. Finally, the mechanical stress-strain analysis is performed, then the next time step occurs, and the process is repeated.

Thermal Model

Calculating the thermal equations is the first step in the model. The thermal equilibrium is established using a fixed point scheme with the Gauss-Seidel method. The

governing differential Equation 4.1 is solved for each sub-domain.

$$\rho C_p \frac{dT}{dt} = \nabla[k\nabla T] + \dot{Q}, \tag{4.1}$$

where ρ is the density of the material, k is the thermal conductivity, C_p is the specific heat of the material, $\dot{Q}$ is a source term, and $\frac{dT}{dt}$ is the derivative of the temperature with respect to time.

Mechanical Model

Constitutive Equations

In the model, there are four distinct stages of solidification, with each one utilizing different constitutive equations:

- Liquid (Newtonian)
- Semi-liquid (Viscoplastic)
- Semi-solid (Elastic-viscoplastic)
- Solid (Elastic-plastic)

The steel is considered semi-solid once it has passed the coherency temperature, which is the temperature at which the metal can be considered solid, which is assumed to be a fraction solid of 0.7 [25].

Viscoplastic Equations

When the steel is in the mushy zone with a solid fraction less than 0.7, a Norton-Hoff [86] viscoplastic constitutive equation is used. This indicates that the

stress is a function of the rate of permanent strain, and the effect of elasticity is neglected in the model [13]. It is shown in Equations 4.2–4.6.

$$\dot{\epsilon} = \dot{\epsilon}^{vp} + \dot{\epsilon}^{th} \tag{4.2}$$

$$\dot{\epsilon}^{vp} = \frac{1}{2K^{evp}(T)}\sqrt{3}\dot{\bar{\epsilon}}^{1-m(T)}\xi \tag{4.3}$$

$$\xi = \sigma + \rho I = \sigma\frac{1}{3}Tr(\sigma)I \tag{4.4}$$

$$\dot{\bar{\epsilon}} = \sqrt{\frac{2}{3}\dot{\epsilon}^{vp}\dot{\epsilon}^{vp}} \tag{4.5}$$

$$\dot{\epsilon}^{th} = (\alpha(T)\dot{T} + \frac{\dot{f}_s(T)\Delta\epsilon_{tr}}{3})I, \tag{4.6}$$

where $\dot{\epsilon}$ is the strain rate tensor decomposed additively into viscoplastic (vp) and thermal strain (th), $K(T)$ is the consistency of the material, $m(T)$ is the sensitivity of the flow stress to the strain rate, α(T) is the coefficient of thermal expansion, and σ_c is the Cauchy stress tensor with a deviatoric part ξ and spherical part ρI. In the liquid phase, the metal is Newtonian and the movements can be such that the inertial terms are dominant because of the low viscosity above the liquidus

Elastic-Viscoplastic Equations

When the steel is in the mushy zone with a solid fraction greater than or equal

to 0.7, a Perzyna with threshold equation is used [65], shown in Equations 4.7–4.10.

$$\dot{\epsilon} = \dot{\epsilon}^{el} + \dot{\epsilon}^{vp} + \dot{\epsilon}^{th} \tag{4.7}$$

$$\dot{\sigma} = E\dot{\epsilon}^{el} = \frac{E}{1+v}\dot{\epsilon}^{el} + \frac{Ev}{(1+v)(1-2v)}Tr(\dot{\epsilon}^{el})I \tag{4.8}$$

$$\dot{\epsilon}^{vp} = \frac{\sqrt{3}}{2\sigma_{eq}}\left\langle \frac{\sigma_{eq}-\sigma_s}{K^{evp}(T)\sqrt{3}} \right\rangle^{\frac{1}{m(T)}} \xi \tag{4.9}$$

$$\sigma_{eq} = \sqrt{\frac{3}{2}\xi : \xi}, \tag{4.10}$$

where E is the fourth order tensor of elasticity, which depends on E_Y, the Young's modulus and ν, Poisson's ratio. σ_s is the plasticity threshold.

Strain Hardening

The strain hardening is taken into account using the equation shown in Equation 4.11.

$$\sigma_{eq} = \sigma_s + K^{evp}(T)\sqrt{3}^{m(T)+1}\ \dot{\overline{\epsilon}}^{m(T)}\ \overline{\epsilon}^{n(T)}, \tag{4.11}$$

where n(T) is the strain hardening exponent.

Solute Model

Solute segregation modelling in THERCAST occurs on two different distance scales:

- Microscopic scale: This is microsegregation, which is the repartition of the chemical elements in the solid and liquid phase along the dendrite arms. Equiaxed grains are not yet taken into account within the model.

- Macroscopic scale: The transfer of chemical elements due to the movement of the liquid, solidification shrinkage, or deformation in the solid along the scale of the slab.

During the calculation, the following assumptions are made:

- The steel is saturated, therefore: $f_{liq} + f_{sol} = 1$ where f_{liq} is the volume fraction of the liquid and f_{sol} is the volume fraction of the solid.
- The liquid is Newtonian, the mushy zone is modelled with viscoplastic behaviour, and the solid zone is modelled with elastic-viscoplastic behaviour.
- The latent heat L is constant.
- At the macroscopic scale, the diffusion in the solid is negligible.

Additionally, during the microsegregation calculation, it is assumed that:

- There is thermomechanical equilibrium of the liquid/solid interface.
- There is perfect diffusion in the liquid.
- The diffusion in the solid can be calculated using a Brody-Flemings model.

Microsegregation Model

Vannier's [87] model of microsegregation is used in addition to the macrosegregation model to translate the non-homogeneous repartition of the chemical elements between the solid and liquid. Using the assumptions outlined, the temperature as a function of liquid composition can be written as shown in Equation 4.12.

$$T = T_{fusion} + \sum_{e=1}^{n} m_{liq}^{r}\ \omega_{liq}^{e}, \tag{4.12}$$

where M_{liq} is the slope of the liquidus. The slopes of the solidus and liquids are related by the partition coefficient, shown in Equation 4.13.

$$\kappa^{e} = \frac{m_{liq}^{e}}{m_{sol}^{e}} \tag{4.13}$$

Introducing a Fourier number F^{e}, the solute concentration in the liquid can be expressed as shown in Equation 4.14.

$$\omega_{liq}^{e} = \omega(1 - (1 - \kappa^{e}F^{e})(1 - f_{liq}))^{-\frac{1-\kappa^{e}}{1-2\kappa^{e}F^{e}}}, \tag{4.14}$$

where ω is the solute concentration, and f_{liq} is the liquid fraction. A Brody-Flemings model is being used, so the Fourier number is input for each element.

Macrosegregation Model

The governing equations for the macrosegregation model are Fourier's law (Equation 4.15) and Fick's law (Equation 4.16) to calculate the heat flux and solute flux, respectively.

$$q = -k\nabla T, \tag{4.15}$$

where k is the thermal conductivity in W m^{-1} K^{-1}

$$J = -D_{liq}^{e}\nabla\omega_{liq}^{e}, \tag{4.16}$$

where D^e_{liq} is the coefficient of chemical diffusion and ω^e_{liq} is the solute concentration of the chemical element in the liquid.

These governing equations are used by THERCAST in conjunction with the results of the thermal model and microsegregation to calculate the macrosegregation.

4.3 Thermal, Mechanical, and Solute Properties of MS1700

4.3.1 Material Properties

For a coupled thermal-mechanical-solute finite element problem, material properties are necessary to describe the process of heat transfer through the system, the stress-strain and solute flow response of the material, and the thermal expansion. The temperatures in the analysis range from the steel pouring temperature (1515℃) to the end of cast temperature (500℃), each property's temperature dependence must also be known. In THERCAST, there is a material property database which contains properties for various metals calculated using JMatPro, a CALPHAD software which calculates material properties. A similar alloy to MS1700, 40cmd8, was used for many of the material properties. The composition of 40cmd8 can be found in Appendix A.1. The evolution of solid fraction was calculated using a thermodynamic computation software, Thermo-Calc.

Thermal Properties

The material properties required for the thermal analysis are the density, heat capacity, and thermal conductivity, latent heat. The latent heat was assumed to be the same as that of 40cmd8, 245 kJ Kg^{-1}. The other thermal properties were calculated based on parametric equations from Meng *et al.* [60], shown in Appendix B, assuming a binary alloy of iron and carbon only. These properties as a function of temperature are shown in Figure 4.2. Indicated at 738 and 1477°C are the phase transitions from alpha to gamma and gamma to delta, respectively. Due to the phases having different thermal properties, these transitions are also accompanied by a change in thermal property. A constant thermal conductivity value of 25 W m^{-2} K^{-1} was used.

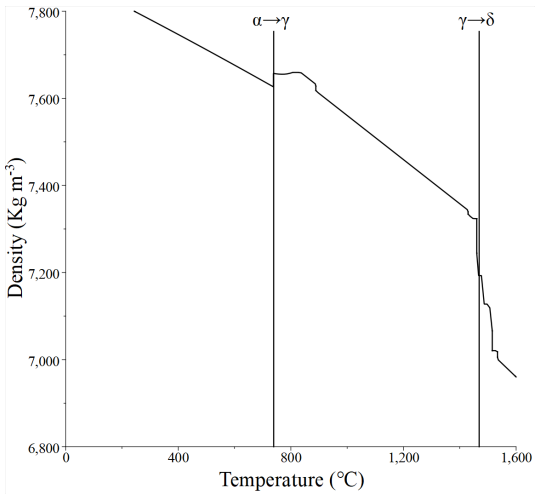

(a) Density

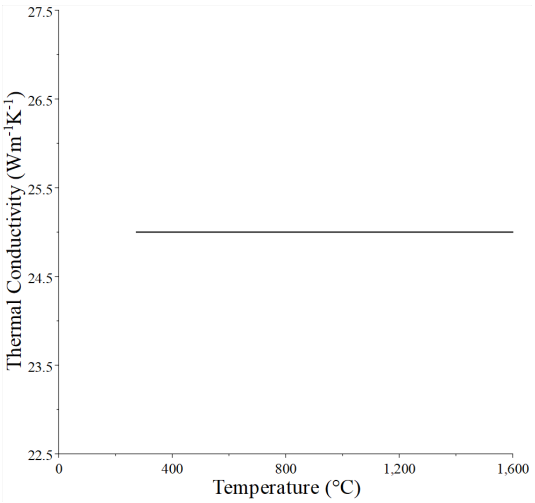

(b) Thermal Conductivity

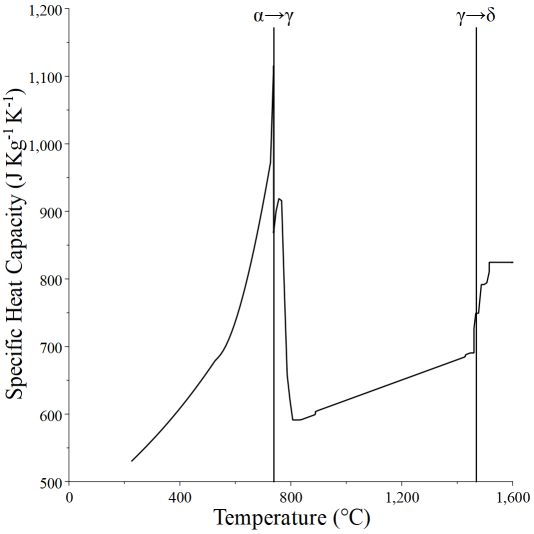

(c) Specific Heat

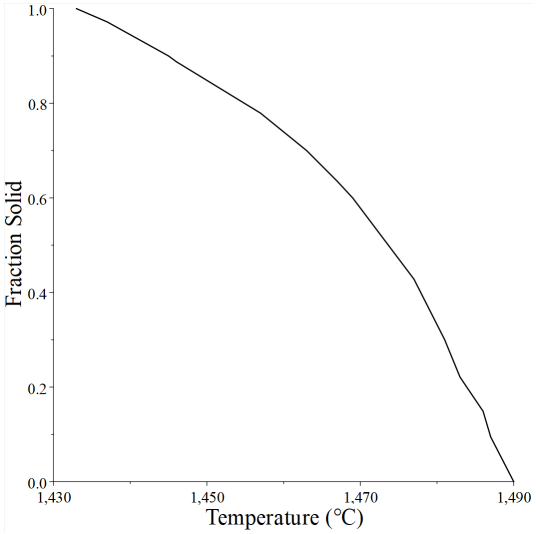

(d) Fraction Solid Evolution

Figure 4.2: Thermal Properties of MS1700, (a) Density, (b) Specific Heat, (c) Thermal Conductivity, (d) Fraction Solid.

Mechanical Properties

The material properties required for the mechanical analysis include the coefficient of thermal expansion, Poisson's ratio, temperature-dependent yield stress, material consistency, and sensitivity to flow stress to strain rate. The Poisson's ratio is assumed to be constant at 0.3. The mechanical properties are shown in Figure 4.3.

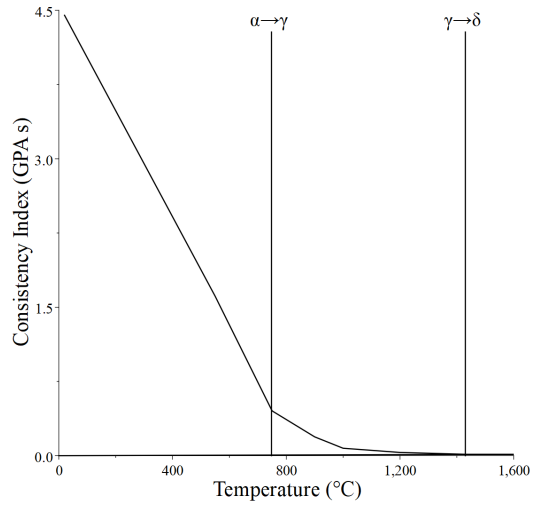

(a) Consistency Index

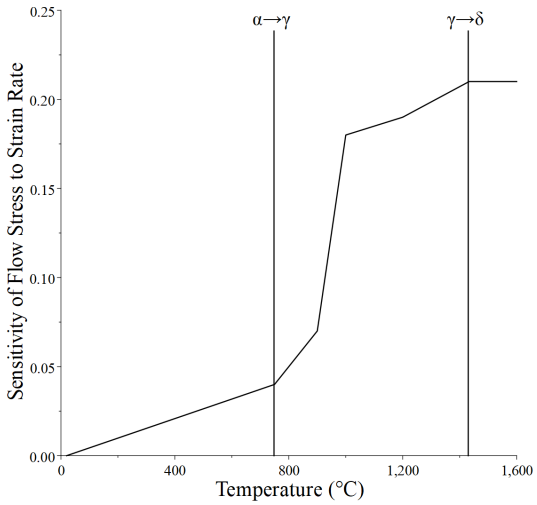

(b) Strain Rate Sensitivity

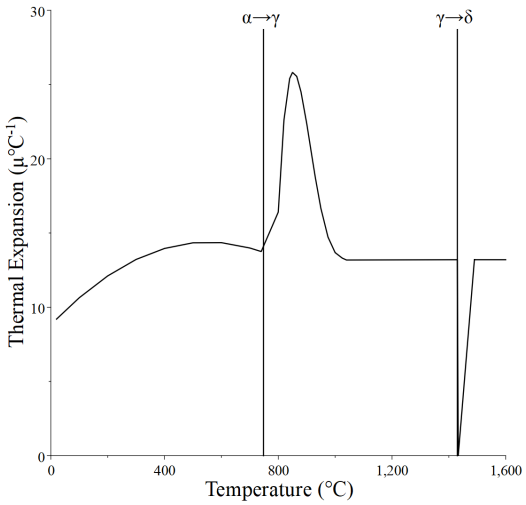

(c) Thermal Expansion

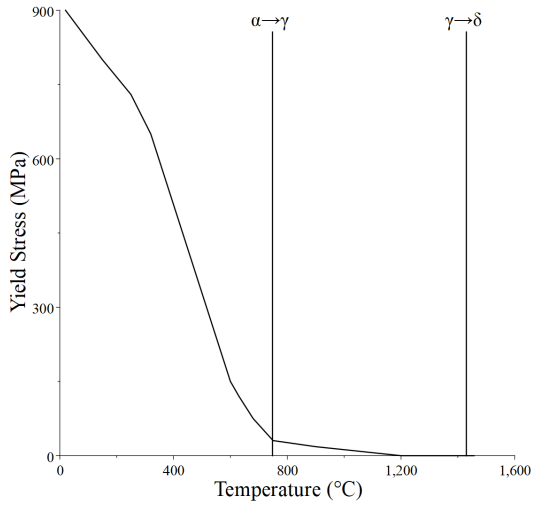

(d) Yield Stress

Figure 4.3: Mechanical Properties of MS1700, (a) Consistency Index, (b) Strain Rate Sensitivity, (c) Thermal Expansion, (d) Yield Stress.

Solute Properties

The material properties required for the solute analysis are the partition ratio, liquidus slope, diffusion coefficient, and Fourier number for each relevant element. These

properties are shown in Table 4.1.

Table 4.1: Solute Properties of MS1700

Element	K	Liquidus Slope (℃/wt%)	Diff. Coeff. (m^2/s)	Fourier Number
C	0.17	-86.1	7.40E-09	0.5
Mn	0.79	-5	3.80E-09	0
P	0.14	-33.5	1.50E-09	0
S	0.03	-33.5	3.00E-09	0
Si	0.72	-18.7	1.24E-09	0

4.4 Model Initial and Boundary Conditions

4.4.1 Initial Conditions

The initial conditions were specified for the steel in the mould and selected based on conventional practices for MS1700. A superheat of 25℃ and a casting speed of 1.0 m/min was used.

4.4.2 Boundary Conditions

The boundary conditions are applied to the exterior faces of the cast slab (broad faces, narrow faces). This condition during primary cooling is a constant HTC. These conditions during secondary cooling are the contact between the steel and the rolls, water-cooled zones, imposed temperature, and convection and/or radiation to ambient air [85]. It is assumed that the steel and the mould are in perfect contact.

Primary Cooling

Thermal boundary conditions were imposed on the steel in the mould. The meniscus surface was assumed to be adiabatic. The mould walls were assumed to impose a constant heat transfer coefficient (HTC) of 5000 $Wm^{-2}K^{-1}$.

Secondary Cooling

In addition to primary cooling in the mould, three cooling zones are used during the secondary cooling model (shown in Figure 4.4):

1. Contact between the steel and the rolls.
2. Heat loss by convection and radiation.
3. Sprayed zones.

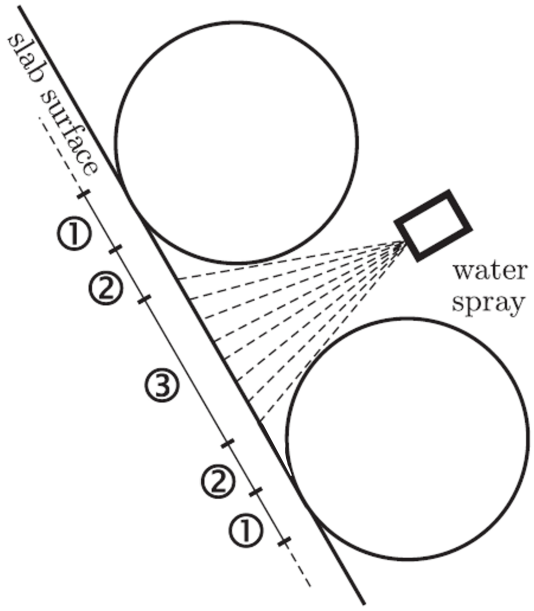

Figure 4.4: Illustration of successive zones of heat loss in secondary cooling
(1) Contact between the steel and the rolls,
(2) Heat loss by convection and radiation,
(3) Sprayed Zones. This figured has been modified from Ref. [64] with permission copyrighted by John Wiley and Sons.

Contact Between Steel and Rolls

The roll heat transfer coefficient between the rolls and the steel was used as a tuning parameter to make adjustments to the heat transfer in the model so that it matched the experimental measurements.

Spray Cooling

Additionally, steel grades are cast with a prescribed amount of spray water cooling throughout the cast length, called a spray plan. The spray plan used for MS1700, Spray Plan A, has an average water flow rate of 133 L/min. The loose side receives less water cooling than the fixed side due to gravity reducing the cooling that the

fixed side receives.

The water spray nozzles spray at a wide angle (α) transversally along the broad face, and at a shallow angle (β) longitudinally along the broad face. A schematic is shown in Figure 4.5. Additionally, there can be multiple sprays for a specified cast length if more cooling is required. Stelco has provided the specifications of the position of each spray nozzle, as well as the α and β angles.

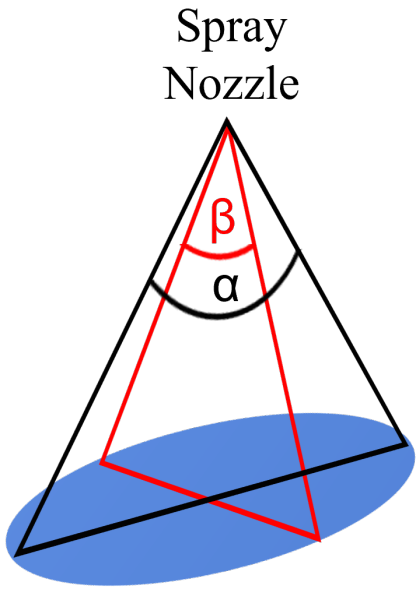

Figure 4.5: Schematic of the water spray nozzle spray pattern. The larger angle, α, and the smaller angle, β, are shown.

The water spray from the nozzles is not uniform, and the spray distribution on the surface of the steel is modelled as a Gaussian distribution to more accurately reflect the physical sprays in the model, shown in Figure 4.6.

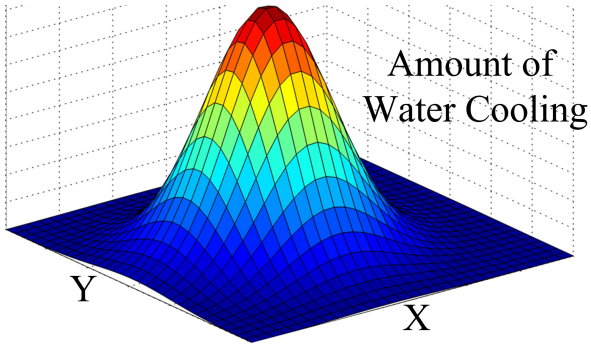

Figure 4.6: Schematic of amount of water spray on the surface of the steel in a Gaussian distribution [1].

Shimada's equation [78] was used for this work as an approximation to calculate the heat transfer from the water spray nozzles to the steel, as described below in Equation 4.17.

$$\alpha(V_S, T_W, \theta) = \frac{1570\ V_S^{0.55}(1 - 0.15cos\theta)(1 - 0.0075T_W)}{f_c}, \tag{4.17}$$

where α is the heat transfer coefficient in W m^{-2} s^{-1}, V_S is the mass flux of water in the sprays in kg m^{-2} s^{-1}, θ is the angle of the slab with respect to the horizontal, T_W is the water temperature of the spray and f_c is a calibration factor dependent of the casting machine. A value of 4 is used for the coefficient.

Convection and Radiation

The ambient temperature was assumed to be 25°C.

The equation for heat transfer by convection and radiation is shown in Equation 4.19.

$$h = h_{cv} + \epsilon_r \sigma (T + T_{ext})(T^2 + T_{ext}^2) \tag{4.18}$$

$$-k\nabla T \cdot n = h(T - T_{ext}), \tag{4.19}$$

where n is the normal vector exterior to the sub-domain, Equation 4.18 is the heat transfer coefficient that results from exchange by convection and by gray-body radiation. h_{cv} is the coefficient of transfer by convection, ϵ_r is the emissivity of the body, σ is the Stefan-Boltzmann constant, equal to 5.67×10^{-8} W m^{-2} K^{-4}, T_{ext} is the exterior temperature.

4.5 Summary

The domain, geometry, material properties, and boundary conditions for the 3D coupled thermal-mechanical-solute of the continuous casting process have been presented. Particularly, the cyclic boundary conditions occurring along the cast length are discussed. To accurately model the change in mechanical conditions during solidification, the constitutive changes from solid to semi-solid to liquid are analysed.

In continuous casting, there are numerous process parameters that affect the quality of the steel. Casting speed and the water spray cooling are the most easily adjustable variables within industry. These variables are also easily adjustable in this model, so their effect on the temperature, solid fraction evolution, stress, and segregation can be evaluated. This allows the simulation to analyse multiple different parameter configurations to improve Stelco's Lake Erie Works casting process rather

than the use of expensive and time-consuming industrial trials.

Chapter 5

Validation of Model Results

In this chapter, the methods with which the thermal model was validated as well as the results of the validation are discussed. The mechanical and solute models have not yet been validated due to problems with the models that are discussed in Chapter 6.

The thermal model was validated by comparing sets of physical measurements to two commonly cast AISI grades, 1005 and 1022, which have a carbon content of 0.05 and 0.20 wt%, respectively. The material thermal properties were calculated based on parametric equations from Meng *et al.* [60], shown in Appendix B, assuming a binary alloy of iron and carbon only. Three sets of physical measurements were used to validate the model:

- Shell thickness at mould exit (Breakout shell measurements).
- Surface temperature measurements during casting (Pyrometers).
- Shell thickness along the cast length (Shim measurements).

5.1 Validation Methods

5.1.1 Shell Thickness at Mould Exit

When there is a severe defect in the mould during casting, it can cause the steel shell to rupture, known as a breakout. When a breakout occurs, the casting must be stopped and the liquid steel flows out from the shell. This results in a steel shell that is of similar thickness as the steel when the breakout occurred, known as a breakout shell. By analysing this shell, the shell thickness during casting can be estimated. Stelco has made a number of such measurements for grades 1005 and 1022.

5.1.2 Surface Temperature

A pyrometer is a thermometer that measures the thermal radiation from a point to measure its temperature from a distance. There are two pyrometers located at the loose side surface of Stelco's Lake Erie Works caster: at strand unbending (14.3 m) and at the end of the cast length (29 m). One set of data was available for 1005 and 1022. A plot of the pyrometer data temperature over time is shown in Figure 5.1. The higher temperature data is the temperature at unbending, and the lower is at the end of cast. The approximate median temperature line is marked on the figure. This data displays a substantial amount of fluctuation caused by process interruptions, process parameter changes, and steam and surface oxide. Additionally, 1005 and 1022 are cast with different spray plans. 1005 uses Spray Plan B, which has an average water flow rate of 139 L/min, and 1022 uses Spray Plan A, which has an average water flow rate of 133 L/min.

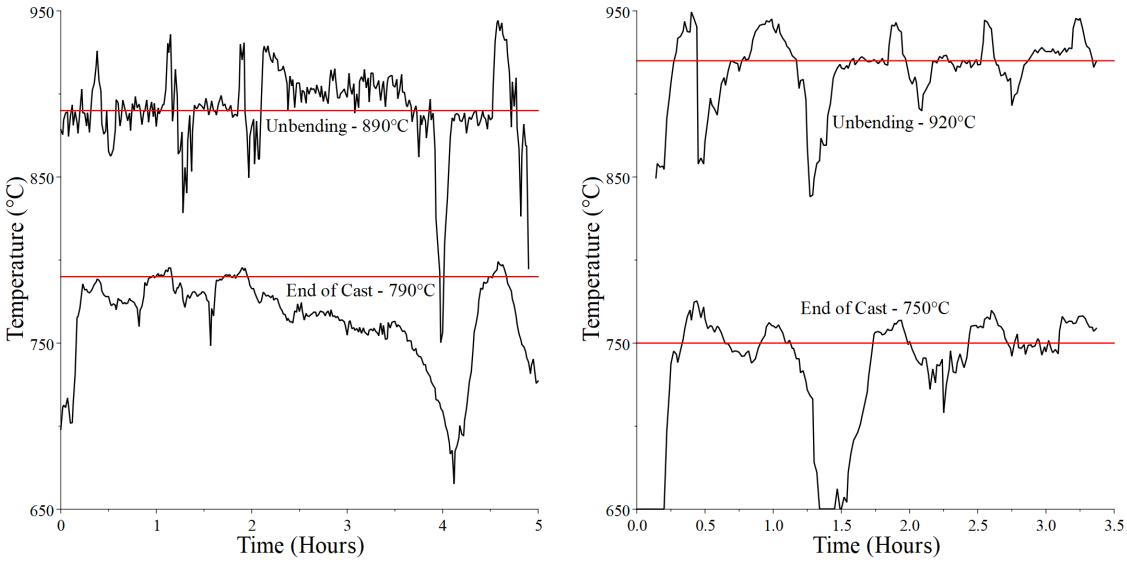

(a) 1005 (b) 1022

Figure 5.1: Pyrometer temperature data showing the variation in temperature during casting at the loose side centre at unbending and end of cast for (a) 1005, and (b) 1022. Approximate median temperature lines are labelled.

5.1.3 Shell Thickness Evolution During Casting

To measure the shell thickness evolution during casting, steel shims are inserted between the strand and the rolls, inducing internal hot-tear cracks. After casting, the steel is cross-sectioned and the tears are measured to determine the shell thickness.

5.2 Validation Results

The casting of these grades were modelled and the surface temperatures were compared to the pyrometer data. The roll heat transfer coefficients were then adjusted such that the surface temperature at the cast lengths measured by the pyrometer and shell thickness evolutions were closest to the predicted values. A comparison

of two roll heat transfer coefficient conditions can be seen in Figure 5.2. Due to a transition from vertical to horizontal casting after unbending and the effect of gravity changing how much water stays on the strand, the start of unbending was used as a transition to a different HTC. The four HTC used are shown relative to each other. Condition A has a relative HTC of 1.0 before unbending, and 0.14 after. Condition B has 0.5 before, and 0.5 after. In the upper figure, the change in surface temperature at the centre of the loose side broad along the cast length is shown. The periodicity displayed on the fixed side and loose side surfaces highlights the thermal cycling that is occurring during the casting process from the changing surface heat transfer. Condition A shows much lower cyclic cooling compared to Condition B due to the lower heat transfer. After unbending, the surface temperature of Condition A continues to decrease at an approximately linear rate, whereas Condition B increases over 5 m, and then stabilises. In the lower figure, the change in fraction solid along the cast length is shown. The shape of the curve is due to the spray cyclic cooling and the changing water flow rate values. Condition A has slower solidification initially, but after unbending, due to the decrease in cooling, Condition A solidifies at the centre before Condition B.

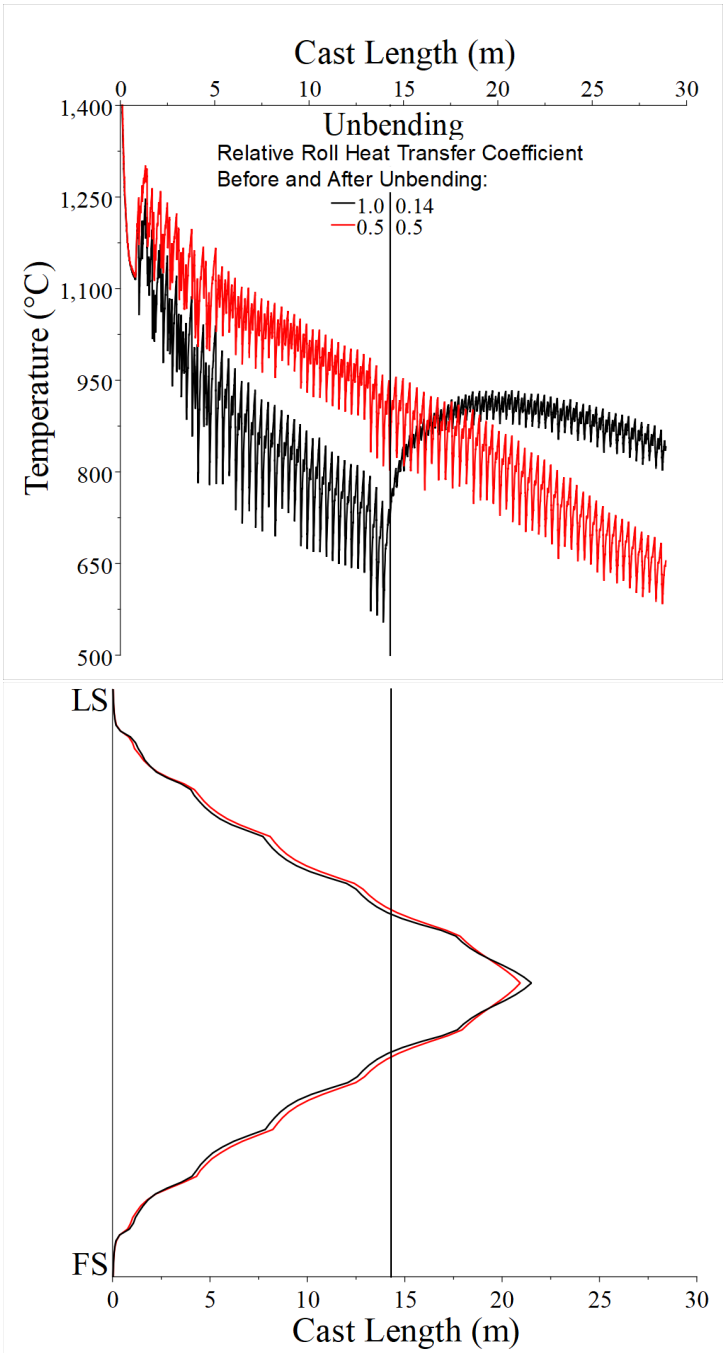

Figure 5.2: Effect of the roll cooling on the surface temperature on the loose side broad face and shell thickness evolution. Shown are two examples with roll cooling before (the first number) and after (the second number) unbending.

5.2.1 Surface Temperature

The resulting predicted change in surface temperatures at the centre of the loose side broad face along the cast length is shown in Figure 5.3 for 1005 and 1022. The predicted temperatures at unbending show good agreement with the measured pyrometer data. At the end of cast the predicted temperature for 1005 and 1022 is within 100℃ of the measured value. This is very good agreement considering the fluctuation in the pyrometer data. The difference can also be due to the multiple sources of error present, such as low experimental sample size, or inaccuracy of the pyrometer temperature measurement caused by steam and surface oxide scale.

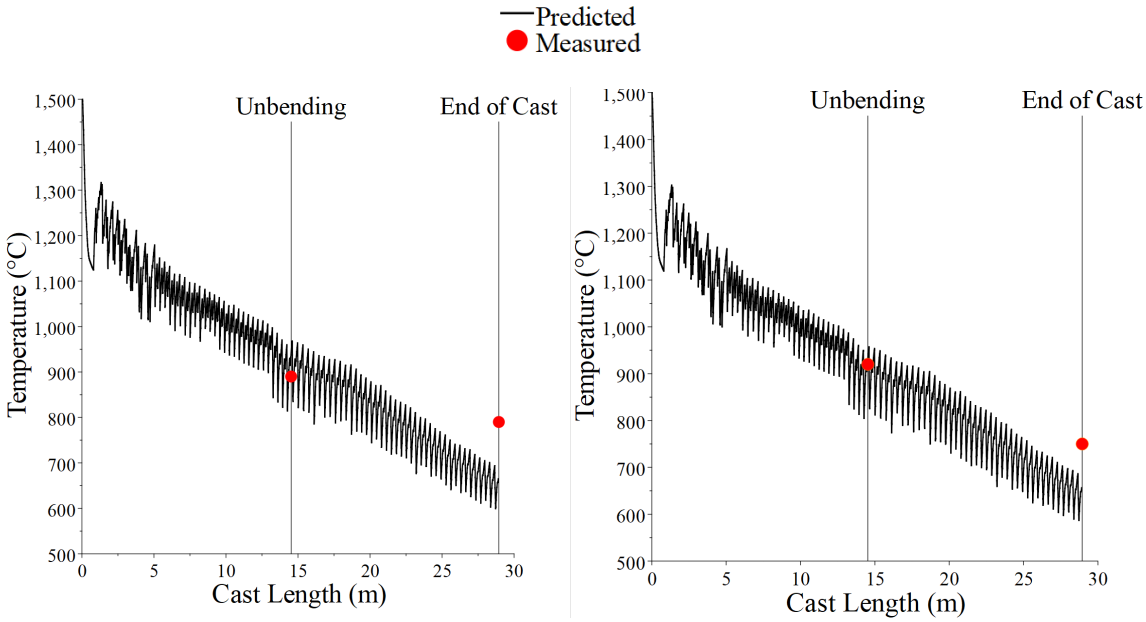

(a) 1005 (b) 1022

Figure 5.3: Comparison of predicted to measured surface temperature measurements for (a) 1005, and (b) 1022.

5.2.2 Shell Thickness Evolution During Casting

The resulting predicted evolution of shell thickness along the cast length was compared to the measured shell thickness. This comparison with 1005 and 1022 is shown in Figure 5.5. 1005, and 1022's predicted shell thickness evolution show excellent agreement with the measured shell thickness evolution.

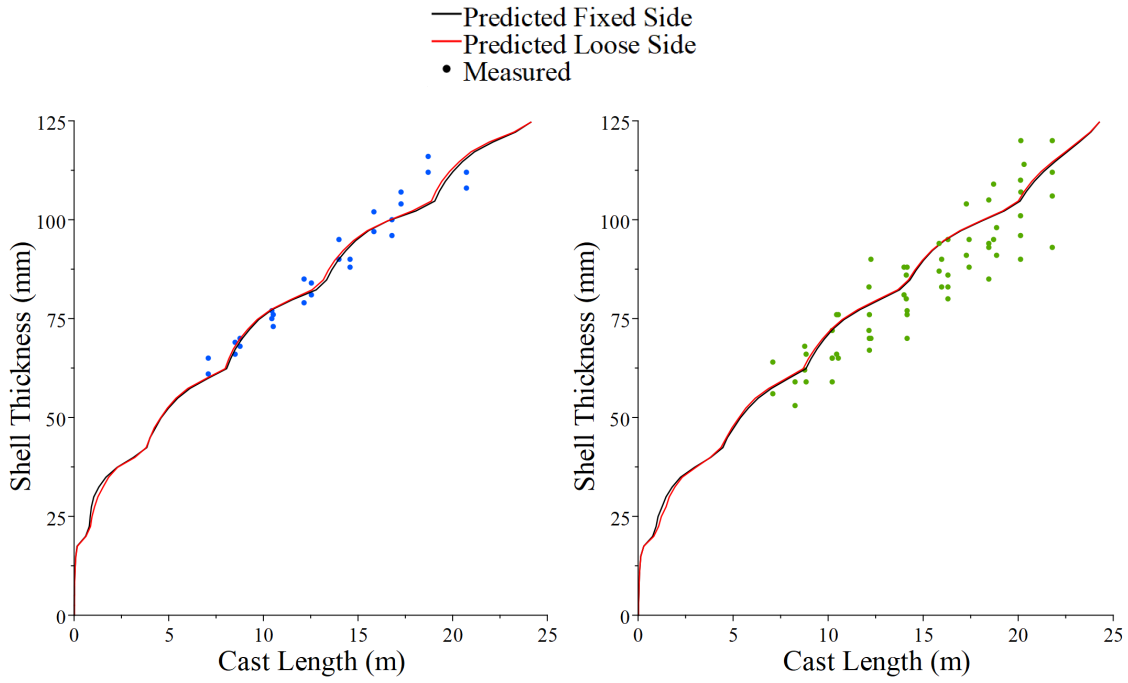

(a) 1005 (b) 1022

Figure 5.4: Comparison of model to measured shell thickness measurements for (a) 1005, and (b) 1022.

5.3 Summary

The thermal model was validated using surface temperature and pyrometer measurements. Good agreement was found with the measured data. This validated model is

a powerful tool for analysing multiple different process parameter configurations to improve Stelco's Lake Erie Works casting process.

Chapter 6

Results & Discussions

6.1 Introduction

In this chapter, the model developed in this thesis is applied to investigate the solidification and surface temperature of Stelco Lake Erie Works' caster. First, in Section 6.2, the evolution of shell thickness is detailed. Next, the evolution of temperature at various points in the slab is shown. Then, the effect of sprays and casting speed on the surface temperature is investigated, and a method to reduce cracking defects is outlined. In Section 6.4, preliminary results of the solute model are given. Lastly, in Section 6.3, preliminary results of the mechanical model are shown.

6.2 Thermal Model

The continuous casting of MS1700 using Stelco Lake Erie Works' caster is simulated with a casting speed of 1.0 m/min. The predicted evolution of shell thickness of MS1700 is shown in Figure 6.1. It was assumed that the steel is sufficiently coherent

to be considered a solid when the solid fraction is greater than 0.7. The upper schematic shows the predicted shell growth along the narrow face centre, and the lower shows schematically the predicted shell growth along the cast length. The model predicts somewhat more cooling on the fixed side compared to the loose side, which is expected from the spray plan. The metallurgical length is 25 m, which is within the expected range of being after unbending to allow ductility, and before the end of cast.

Shown in Figure 6.2 is a schematic of the predicted shell growth along the broad face centre. It can be seen that the final solidification point is very close to the edge surface of the steel. This is because unlike the broad face, which has spray cooling throughout the cast length, the narrow face has no direct cooling after 1 m of casting. This leads to very little cooling occurring on the narrow face, while the broad face has a significant amount of cooling due to the water sprays and rolls.

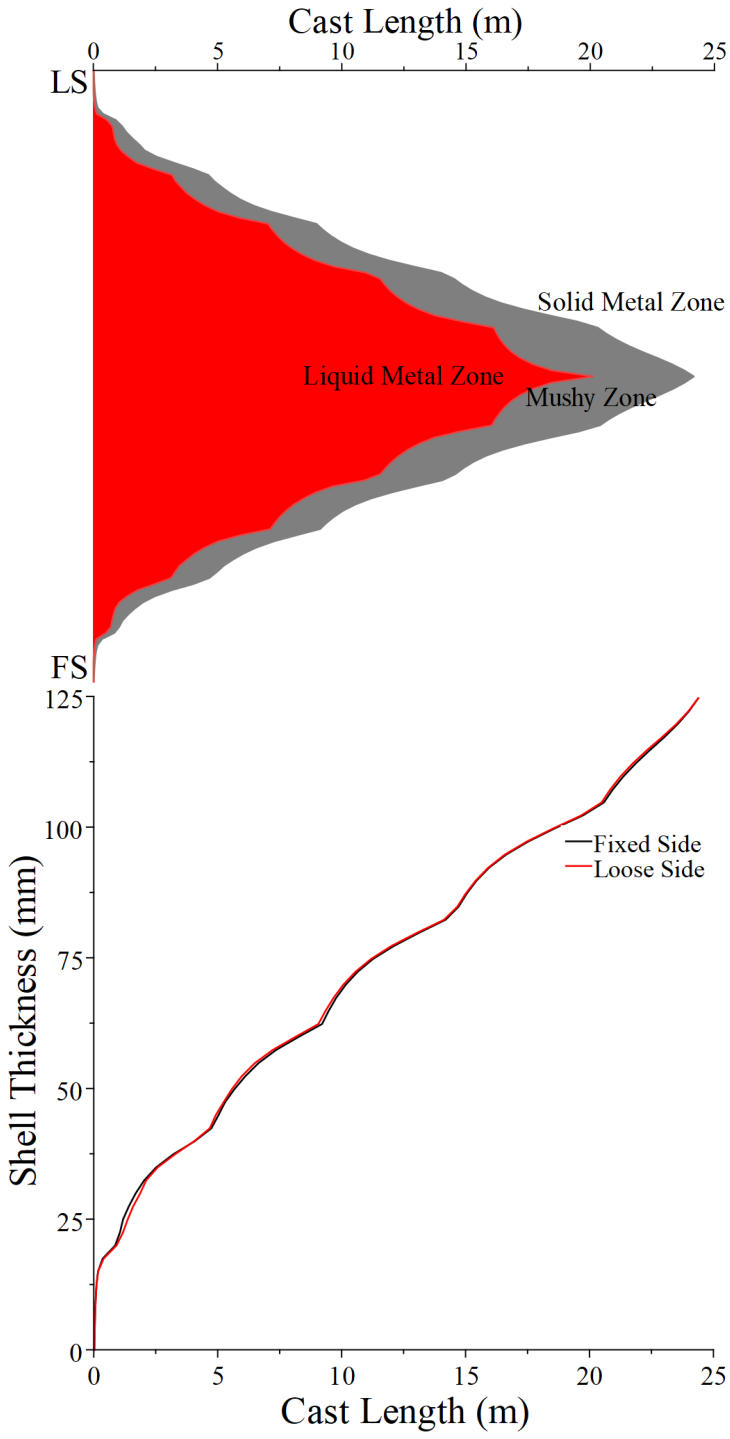

Figure 6.1: Upper: Schematic of predicted shell growth along the narrow face centre. Lower: Predicted evolution of shell thickness along the cast length.

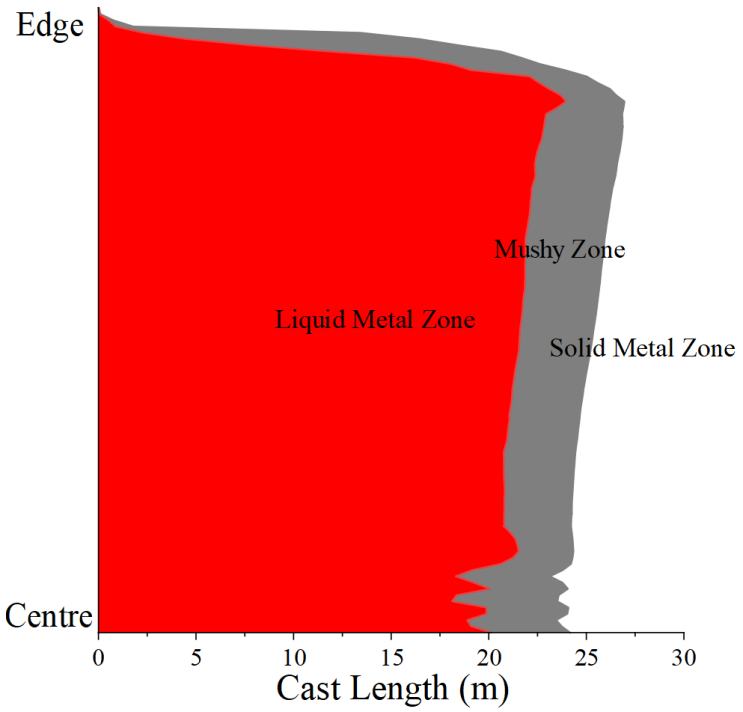

Figure 6.2: Schematic of predicted evolution of shell thickness along the broad face centre.

6.2.1 Evolution of Temperature Along Cast Length

A plot of the predicted evolution of temperature at the centre, loose side surface, and fixed side surface is shown in Figure 6.3. Initially, the spray cooling difference between the fixed and loose side is very high, leading to markedly different surface temperatures. However, after approximately 4 m of cast length, the spray cooling decreases, causing the fixed and loose sides to have very similar surface temperatures. The temperature at the centre displays very little change until approximately 25 m when the steel has solidified, at which point the temperature rapidly decreases.

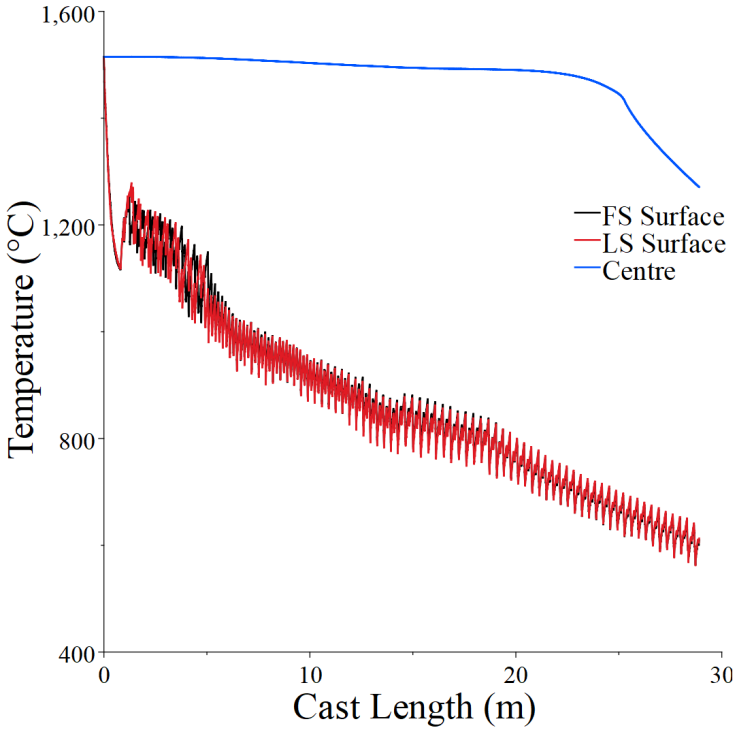

Figure 6.3: Predicted evolution of temperature at the centre, loose side surface, and fixed side surface.

6.2.2 Evolution of Surface Temperature During Unbending

Next, the evolution of temperature during the unbending section, where the stress on the strand is highest and therefore where cracks are most likely to form, was investigated. Shown in Figures 6.4 is the evolution of surface temperature from the beginning of unbending to the end (14.3–19 m) along the loose and fixed side broad face. The black lines indicate the position of the centre of the rolls. The thermal cycling is clearly displayed by the significant change in temperature at the moment the roll comes into contact with the steel. Additionally, the effect of the water spray cooling on the surface of the strand can be observed. The temperature is higher at the edge and lower at the centre due to the lack of spray cooling at this point. The

temperature on the loose side is marginally higher than the fixed side due to it having more spray cooling.

Shown in Figure 6.5 is the evolution of surface temperature during unbending along the narrow face. It should be noted that the temperature scale is different from the broad face profile due to the higher temperature. It can be observed that the temperature at the centre of the narrow face is extremely hot due to a lack of direct cooling on the narrow face during casting. The roll cooling effect can be seen as well on the narrow face, as there is a decrease in temperature due to corner cooling on the edge of the broad faces.

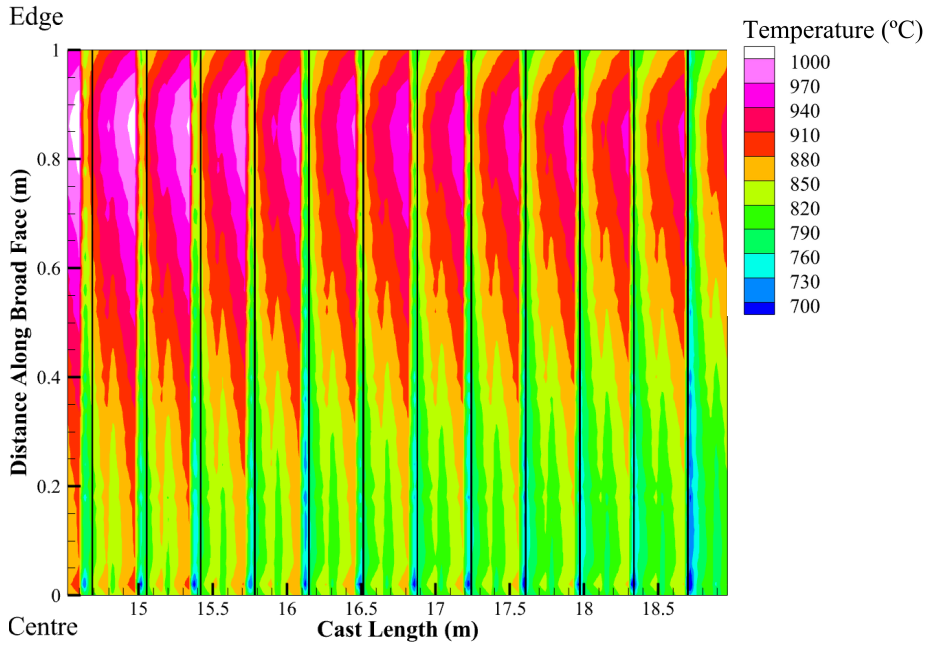

(a) Loose Side

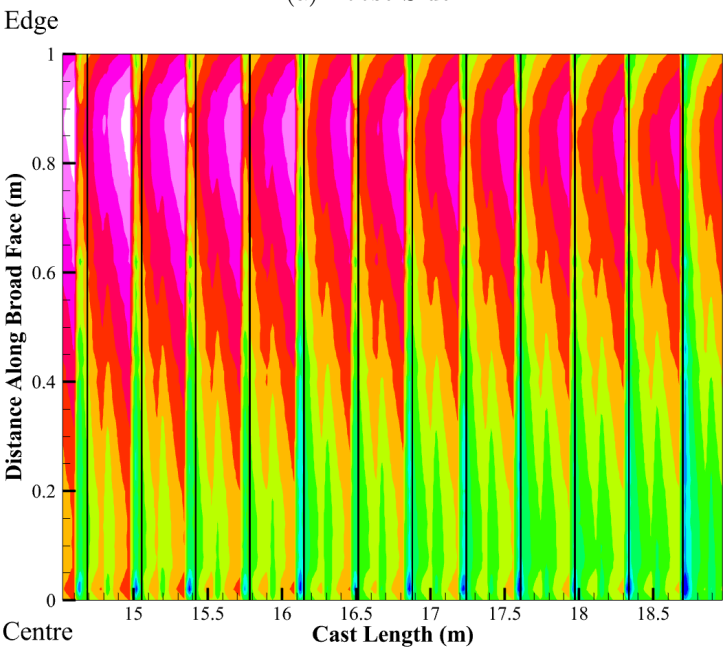

(a) Fixed Side

Figure 6.4: Surface temperature profile along the broad face unbending region on the (a) Loose Side and (b) Fixed Side.
The black lines indicate the position of the rolls.

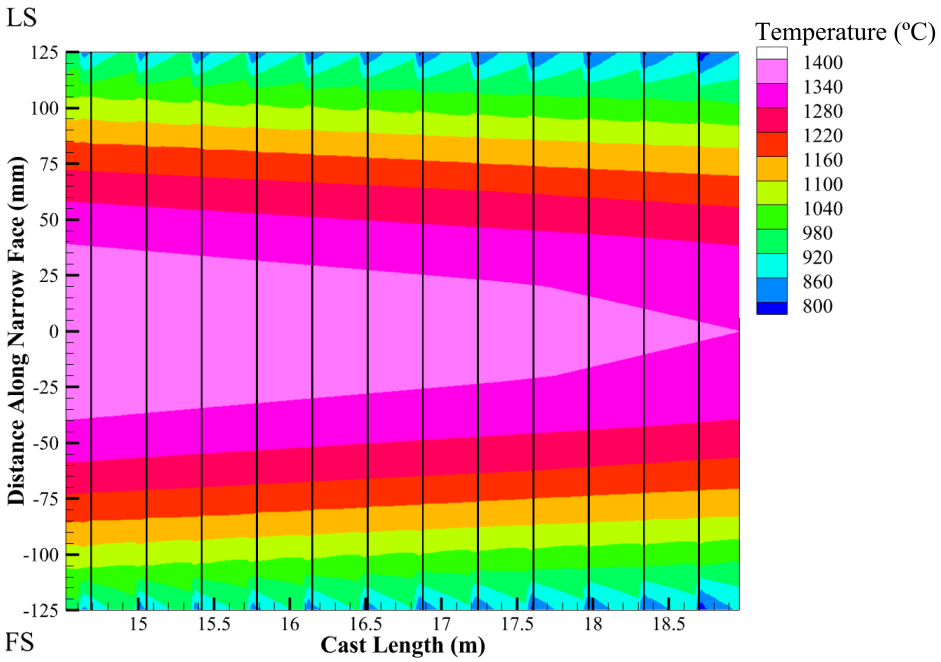

Figure 6.5: Surface temperature profile within the ductile temperature region along the unbending region on the narrow face.
The black lines indicate the position of the rolls.

6.2.3 Susceptibility of Cracking

Using the thermodynamic computation software Thermo-Calc, the low ductility region for MS1700 can be estimated. Assuming that the region exists between the Ar3 (starting temperature for transformation of austenite into ferrite during cooling [107]) and Ac3 (the final critical temperature at which ferrite is completely transformed into austenite during heating) temperatures [109], the low ductility region can be estimated as 738–805°C. Thus, the previous figures of the broad face surface temperature during unbending are shown again in Figure 6.6. However, the temperature scale is adjusted to the range of the Ar3–Ac3 temperatures for MS1700, 738–805°C, highlighting the areas which are more likely to suffer transverse cracks. With this scale, it can be

seen that the centre is predicted to be the most susceptible to cracking, and the loose side is more susceptible than the fixed side. The areas that are most susceptible to cracking occur immediately before and after the roll due to a lack of cooling in these areas. This was repeated for the narrow face, however, due to the high temperature on the narrow face, the majority of the face is not within the low ductility region during unbending.

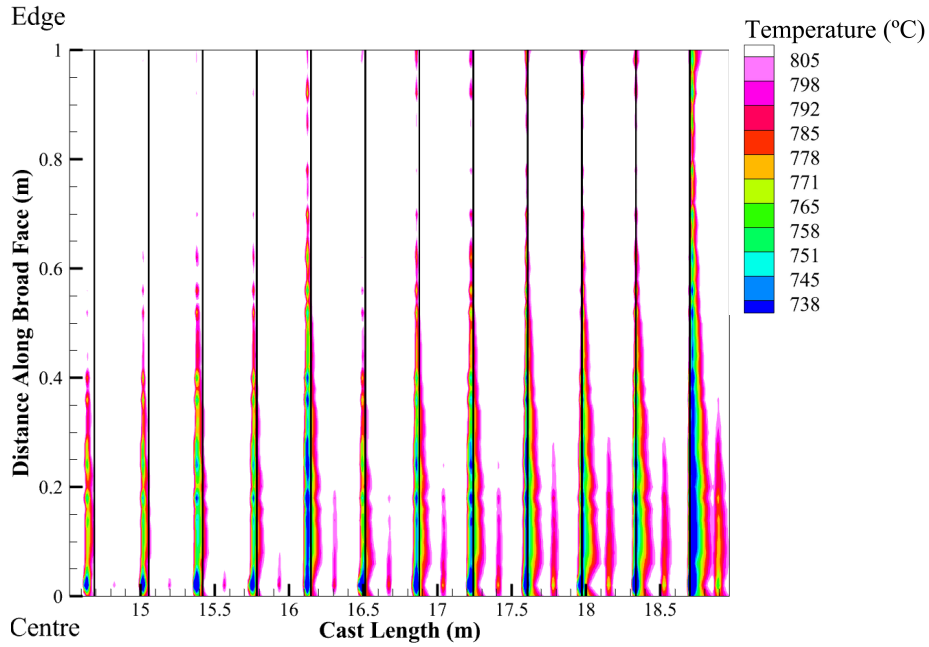

(a) Loose Side

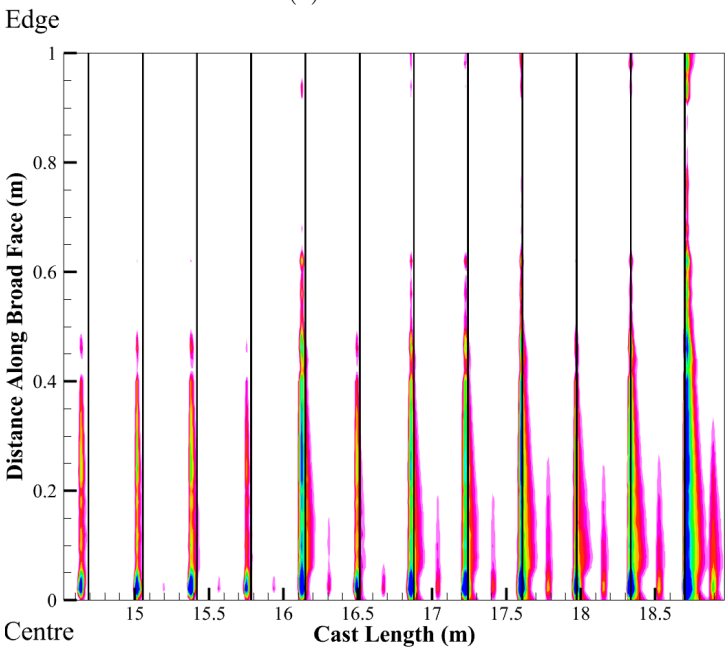

(a) Fixed Side

Figure 6.6: Surface temperature profile within the ductile temperature region along the unbending region on the (a) Loose Side and (b) Fixed Side.
The black lines indicate the position of the rolls.

Effect of Casting Speed and Water Spray

In this section, the effect of the casting speed and water spray cooling on the surface temperature at unbending is explored. The analysis of the unbending section was repeated with a total water flow that is 100, 90, 80, and 60% of the base amount, and a casting speed of 1.05, 1.1, 0.95, and 0.9 m/min. As a metric to measure the degree of susceptibility of transverse cracking, each data point which is between 738 and 805℃ was counted and this was divided by the total number of data points, thus giving the area of the unbending region that is in the ductility trough. The results are summarized in Table 6.1. It can be seen that the loose side is more susceptible to cracking than the fixed side. As the spray cooling decreases, the metallurgical length increases. However, the largest factor that affected the metallurgical length was the casting speed. The maximum possible metallurgical length is 29 m, however, due to variance in the casting conditions, it is unsafe to have a predicted metallurgical length that is close to this value because it can cause significant damages to the machine if the metal is not completely solidified.

Table 6.1: Analysis of the effect of casting speed and spray cooling on the area of the unbending region that is within the ductility trough (738–805℃) on the fixed side, loose side and narrow face.

V_C (m/min)	Spray Cooling (%)	Area in Ductile Trough (%)		Met Len (m)
		FS	LS	
0.95	100	14	18	22.9
0.95	90	12	16	23.1
0.95	80	10	14	23.3
0.95	60	7	10	23.7
1.00	100	12	15	24.2
1.00	90	10	13	24.3
1.00	80	8	11	24.5
1.00	60	5	8	24.9
1.05	100	13	15	25.4
1.05	90	11	13	25.6
1.05	80	9	11	25.8
1.05	60	6	8	26.2

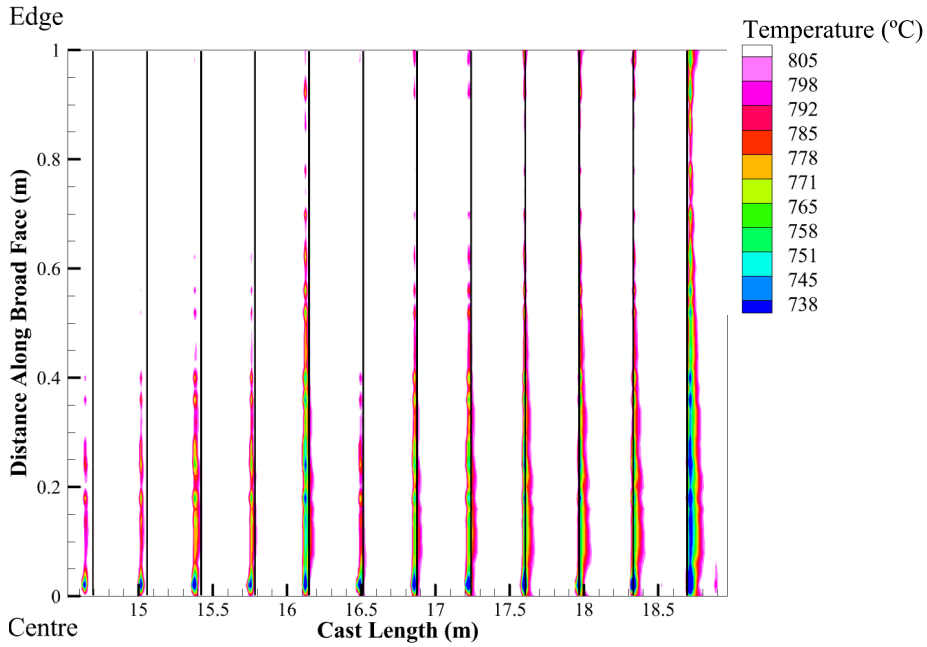

(a) 60% baseline water spray

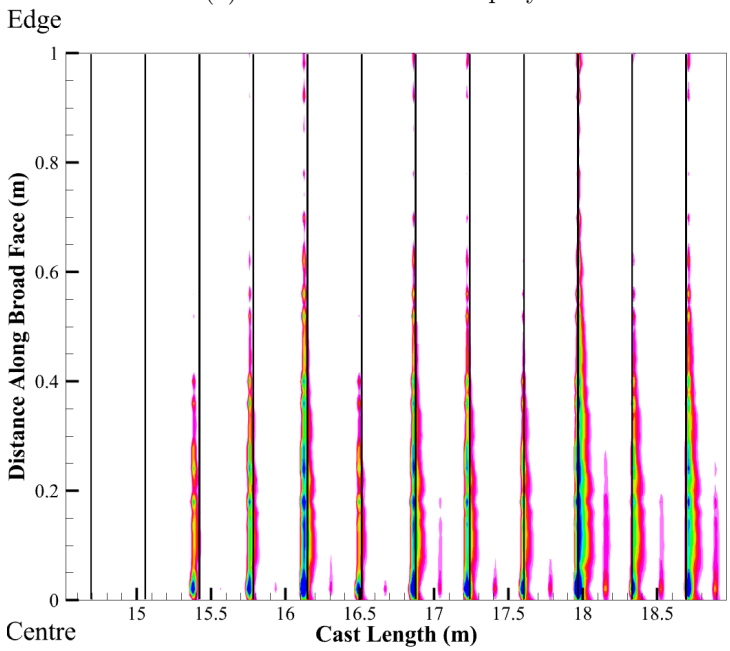

(a) 1.05 m/min casting speed

Figure 6.7: Surface temperature profile along the unbending region on the loose side broad face with conditions of (a) 60% baseline water spray and (b) 1.05 m/min casting speed.

A DOE analysis was done using this data. The main effects plot for the percentage of the broad face area in the ductile trough temperature region is shown in Figure 6.8. It shows that there is a very small decrease in the susceptibility to cracking as the casting speed is increased to 1.05 m/min, and a decreasing susceptibility as the spray cooling is decreased. Although the fixed side has a moderately higher response to increasing casting speed compared to the loose side, the response to water spray amount is the same on both broad faces. The DOE analysis predicts that the cracking susceptibility would be minimized with a casting speed of 1.0 m/min and a water spray of 60% or lower. However, this also extends the metallurgical length, which can lead to more serious defects such as a rupture of the steel shell if not managed correctly. Therefore, further analysis would be required to determine proper safety factors during casting.

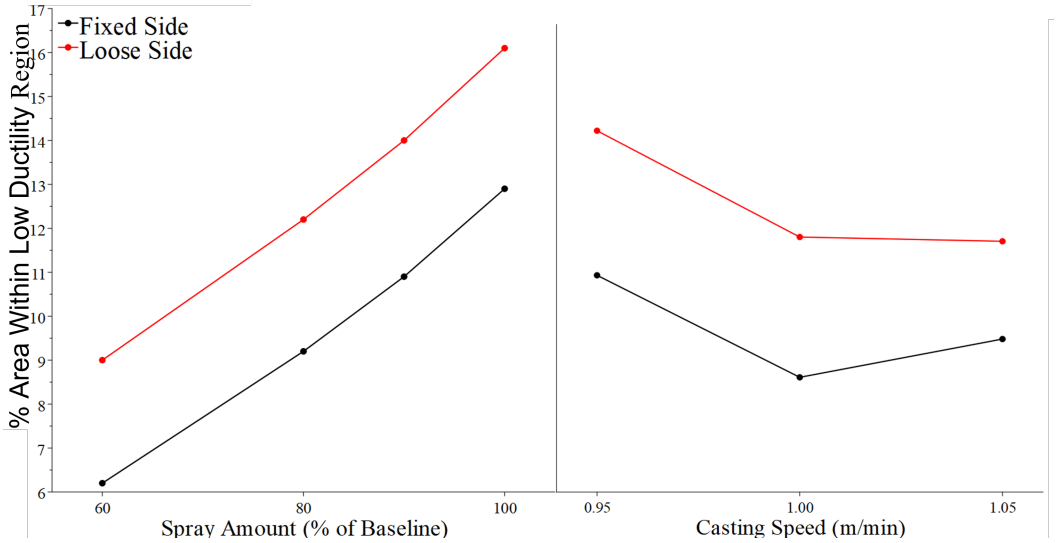

Figure 6.8: Main effects plot of casting speed and amount of water spray on the area of the broad face that is within the ductile trough temperature region.

6.3 Mechanical Model

A mechanical model was also created, using the parameters outlined in Chapter 4, with a superheat of 25℃ and a casting speed of 1.0 m/min. It should be noted that the roll heat transfer coefficient values are different from what was used for the thermal model due to time constraints. The surface temperature and mechanical stress during unbending on the loose and fixed side is shown in Figure 6.9 and Figure 6.10, respectively. Although the roll cooling is very similar on the loose and fixed side, there is a large difference in the surface temperature and mechanical stress. The contact of the rolls can clearly be seen at each roll position on the fixed side, however, this is not present on the loose side. This indicates that during the model calculation, there was an error which caused the position of the steel slice to move, preventing the rolls from coming into contact with the loose side. This issue aside, the model is predicting stresses on the order of 40 MPa, which exceed the yield strength of 20–30 MPa. These preliminary results predict that there is susceptibility of cracking due to the impingement of the rolls on the steel. Many of the high stress regions occur near the centre of the slab, although there are also regions of high stress near the edge, which in addition to the higher temperature and stress concentration there, can lead to cracking.

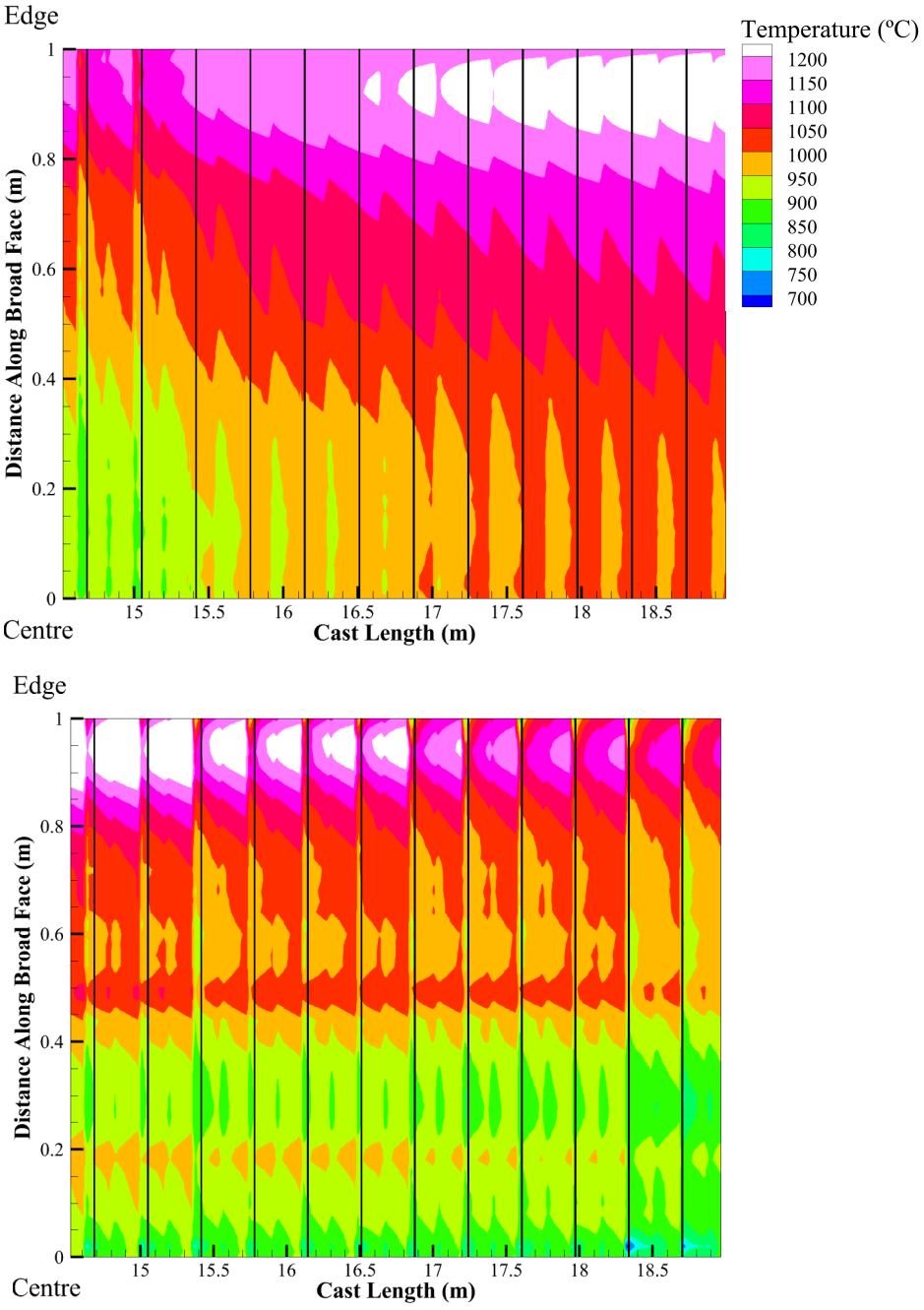

(a) Fixed Side

Figure 6.9: Surface temperature profile during unbending along the (a) Loose Side and (b) Fixed Side.
The black lines indicate the position of the rolls.

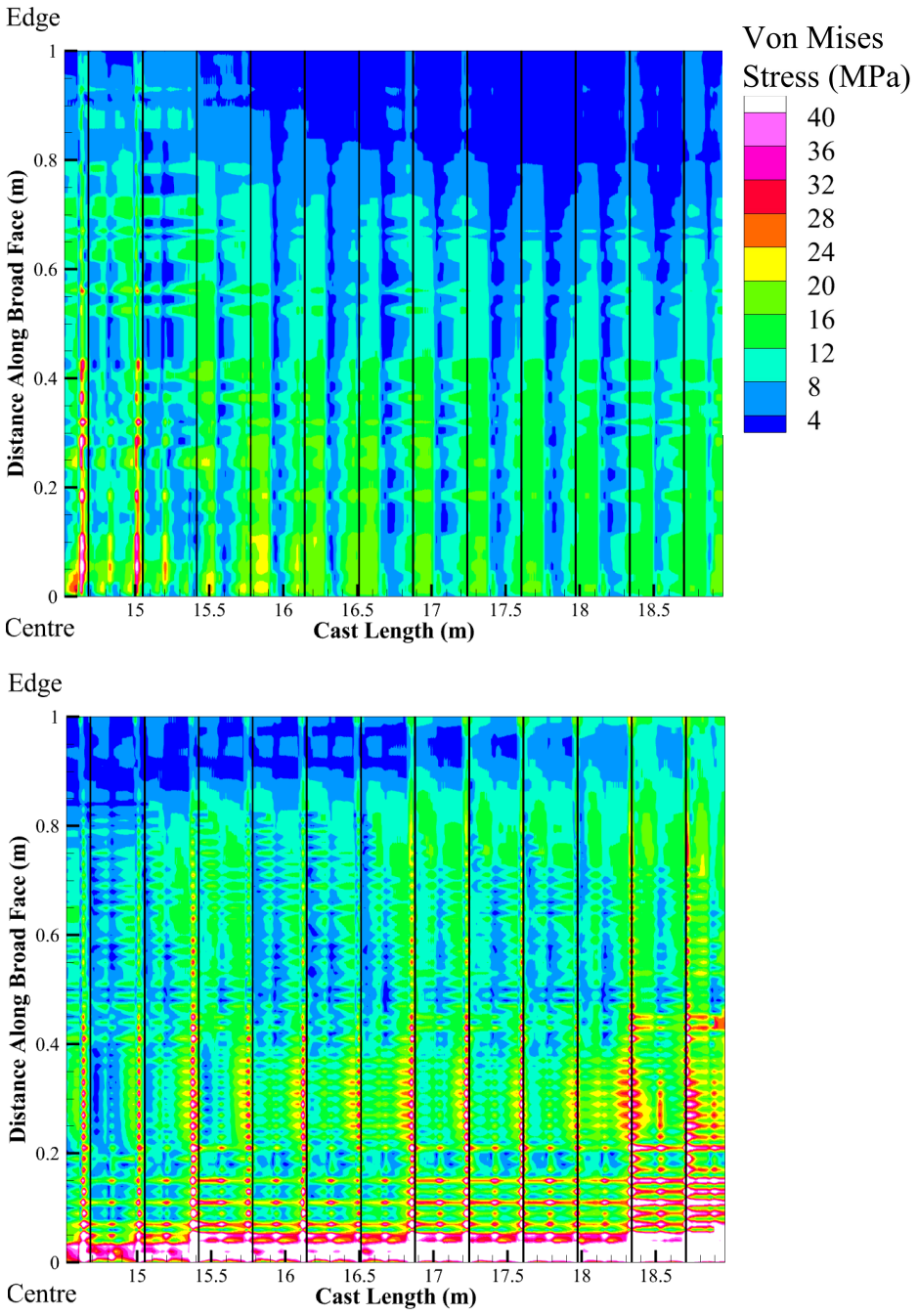

(a) Fixed Side

Figure 6.10: Von Mises stress during unbending on the (a) Loose Side and (b) Fixed Side.
The black lines indicate the position of the rolls.

6.4 Solute Model

A solute model was created using the parameters outlined in Chapter 4, with a superheat of 25℃ and a casting speed of 1.0 m/min. The segregation profile on the narrow face centre along the cast length is shown in Figure 6.11. It predicts negligible segregation from the bulk value of 1.2 Mn wt%. However, there is still an expected trend of solute movement towards the centre, and the centreline has the highest concentration. This indicates that there is not enough solute transport that is occurring in the model.

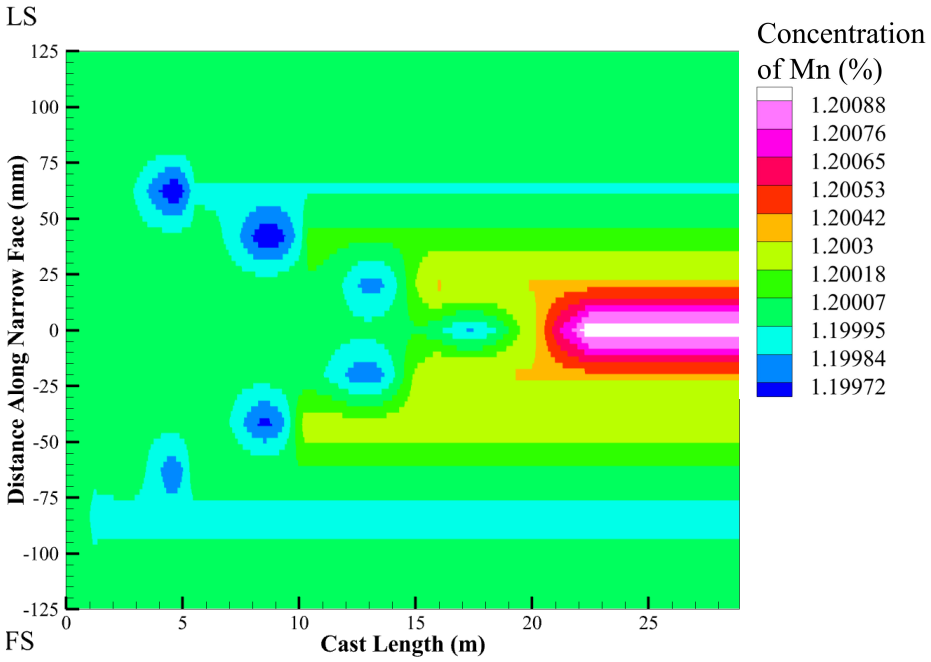

Figure 6.11: Segregation profile of manganese on the narrow face centre along the cast length.

Chapter 7

Conclusion

This chapter provides key contributions of the thesis, followed by an outline of the major limitations of the current model and suggestions for future work, particularly for the prediction of defects during continuous casting.

7.1 Conclusions

The key objectives that were completed in this work can be summarized as follows: A 3D thermal steel continuous casting model has been made for Stelco's Lake Erie Works caster. The model was created using THERCAST, and was validated using experimental measurements. The model was then applied to investigate the evolution of temperature and solid fraction along the cast length. It was found that decreasing the cast speed increased the susceptibility to cracking during the unbending region, and increasing the cast speed has a negligible effect. It was determined that decreasing the amount of water spray cooling reduced the susceptibility to cracking during

the unbending region, however, this is also accompanied by an increase in metallurgical length, so further work is required to determine appropriate safety factors to ensure the steel is completely solidified. Preliminary results of solute and mechanical models were discussed, and further work is required to improve the limitations of these models.

7.2 Model Limitations & Potential Future Work

7.2.1 Model Limitations

The critical model assumptions and the limitations of the current model are discussed in addition to potential future works.

1. The current model focuses on secondary cooling for computational efficiency. However, defects such as transverse cracking may initiate in the mould and be exacerbated during secondary cooling. Therefore, to more effectively predict defects, a more robust primary cooling model may be utilized.

2. The current model assumes that the excess water cooling can be accounted for by increasing the cooling on the rolls. This is accurate in the upright section of the caster, however, after unbending, it may be more accurate to adjust this value and increase ambient cooling rather than the roll cooling, reducing the periodicity of the cooling.

3. The solute model currently predicts a negligible amount of segregation. This is likely due to inaccurate material property data being used in the model,

however, further research is required to determine which parameters should be changed to increase the predicted solute transport.

4. The mechanical model presents problems with the rolls not impacting the steel during unbending, drastically reducing the cooling and the mechanical stress experienced by the steel. Further work is required to investigate and amend these issues.

5. Currently, the formation of oscillation marks is not considered in the model. Stress concentration due to oscillation marks is a key factor in the formation of transverse cracks, thus including this effect in the model would allow it to more accurately predict the formation of cracks during secondary cooling.

6. In the macrosegregation model, the development of the grain structure is currently not taken into account. Since transverse cracking is heavily dependent on the microstructure, grain structure modelling would improve the prediction of transverse cracking.

7.2.2 Future Work

The validated thermal model developed in this thesis also has many future applications to aid Stelco Lake Erie Works in improving the continuous casting process. Some of these applications are described below.

1. Exploring the casting of more grades. MS1700 was the focus of this work, but the other grades can be used in the model if their material properties are known. Grades such as ultra low carbon which also present casting difficulties would benefit greatly from insight through modelling.

2. Examining the effect of slab width on the proclivity for transverse cracking. Altering the slab width will affect the amount of water spray that is applied to the edge of the slab, and will thus affect its tendency to be in the low ductility temperature region during unbending.

3. Investigating the effect of disruptions in casting equipment such as roll locking or blocked spray nozzles. These are common disruptions that occur during casting, and the model can be used to investigate the extent of the impact of these disruptions on the casting process.

Additionally, future work includes the improvement of the mechanical and solute models. Presently, during the mechanical model calculation, due to an error during calculation, the steel slice moves, preventing the loose side broad face from coming into contact with the rolls. Despite this, the model is predicting stresses on the order of 40 MPa on the fixed side, which exceed the yield strength of 20-30 MPa, indicating that there is susceptibility to cracking due to the impingement of the rolls. The solute model predicts negligible segregation along the centreline. However, there is still an expected trend of solute movement towards the centre, and the centreline has the highest concentration.

By overcoming the limitations described above and improving the mechanical and solute models, the current model can be further expanded to become a more advanced predictive tool for defect formation and process knowledge gathering. By using this model, it can help steelmakers to optimize the process parameters to reduce defects and improve the overall quality of the steel.

Appendices

Appendix A

Material Composition

Table A.1: Composition of 40cmd8 (wt.%).

Element	Fe	C	Mn	Cr	Mo	Si
Composition (wt.%)	95.6	0.4	1.5	2	0.2	0.3

Appendix B

Material Property Calculations

Heat Capacity

The equations for heat capacity are shown below:

$$C_p^{\alpha} = \begin{cases} 504.8146 - 0.1311139T(K) - 5.1875834 \times 10^6 T(K)^{-2} & \\ +4.486659 \times 10^{-4} T(K)^2 & T(K) \leq 800 \\ -4720.324 + 4.583364T(K) + 1.109483 \times 10^9 T(K)^{-2} & 800 < T(K) \leq 1000 \\ -11501.07 + 12.476362T(K) & 1000 < T(K) \leq 1042 \\ 34871.21 - 32.02658T(K) & 1042 < T(K) \leq 1060 \\ -10068.18 + 5.98686T(K) + 5.217657 \times 10^9 T(K)^{-2} & 1060 < T(K) \leq 1184 \end{cases}$$

$$C_{\gamma}^{p} = 429.8495 + 0.1497802T(K)$$

$$C_{l}^{p} = 824.6157$$

Density

The equations for density are shown below:

$$\rho(T) = \rho_\alpha f_\alpha + \rho_\delta f_\delta + \rho_\gamma f_\gamma + \rho_l f_l$$

$$\rho_\alpha = 880.76 - 0.3244T - 2.7461 \times 10^{-5} T^2$$

$$\rho_\delta = (8010.71 - 0.4724T)(1 + \frac{Cpct}{100 - Cpct})(1 + 13.43 \times 10^{-3} Cpct)^{-3}$$

$$\rho_\gamma = (8105.91 - 0.5091T)(1 + \frac{Cpct}{100 - Cpct})(1 + 8.317 \times 10^{-3} Cpct)^{-3}$$

$$\rho_l = 7965.98 - 0.619T$$

Thermal Conductivity

A constant value of 25 Wm^{-1} K^{-1} was used for thermal conductivity.

Bibliography

[1] shabbychef (https://stats.stackexchange.com/users/795/shabbychef), *Plot two-dimensional gaussian density function in matlab*. [Online]. Available: https://stats.stackexchange.com/q/102734.

[2] AISI, *Steel offers durable, cost-effective solutions for automotive vehicles*, 2020. [Online]. Available: https://www.steel.org/steel-markets/automotive/.

[3] AIST, *The Making, Shaping and Treating of Steel, 11th Edition, Casting Volume*, 11th ed., A. Cramb, Ed. Association for Iron & Steel Technology, 2003, ISBN: 978-0-930767-04-4.

[4] N. Amratav, K. Kumar, and M. Pillai, "Computer simulation of continuous casting processes: A review," *Advances in Materials*, vol. 10, p. 31, 3 2021, ISSN: 2327-2503. DOI: 10.11648/j.am.20211003.11.

[5] L. Anand, "Constitutive equations for the rate-dependent deformation of metals at elevated temperatures," *Transactions of the ASME*, vol. 104, pp. 12–17, 1982.

[6] ArcelorMittal, "MartINsite® steels," 2013. [Online]. Available: https://automotive.arcelormittal.com/products/flat/martensitic_steels/martinsite.

[7] W. S. Association, "World steel in figures 2021," 2021, pp. 8–9.

[8] K. Bachman, *Lightweighting still dominates great designs in steel seminar*, Mar. 2018. [Online]. Available: https://www.thefabricator.com/stampingjournal/article/stamping/lightweighting-still-dominates-great-designs-in-steel-seminar.

[9] N. Baluch, Z. M. Udin, and C. S. Abdullah, "Advanced high strength steel in auto industry: An overview," *Engineering, Technology & Applied Science Research*, vol. 4, pp. 686–689, 4 2014.

[10] H. G. Baumann and G. Schäfer, "Beitrag zur berechnung der kontraktion von stahl während seiner erstarrung," *Archiv für das Eisenhüttenwesen*, vol. 41, pp. 1111–1115, 12 1970.

[11] C. Beckermann, "Modelling of macrosegregation: Applications and future needs," *International Materials Reviews*, vol. 47, pp. 243–261, 5 2002.

[12] M. Bellet, "3d finite element thermomechanical modelling of the primary cooling for beam-blanks continuous casting," pp. 1220–1229, June 2014.

[13] M. Bellet, O. Cerri, M. Bobadilla, and Y. Chastel, "Modeling hot tearing during solidification of steels: Assessment and improvement of macroscopic criteria through the analysis of two experimental tests," *Metallurgical and Materials Transactions A*, vol. 40, pp. 2705–2717, 11 2009. DOI: 10.1007/s11661-009-9955-5.

[14] E. Brandaleze, G. D. Gresia, L. Santini, A. Martn, and E. Benavidez, *Mould Fluxes in the Steel Continuous Casting Process*. InTech, Sep. 2012, vol. 233, pp. 205–233, ISBN: 978-953-51-0774-3. DOI: 10.5772/50874.

[15] J. K. Brimacombe and K. Sorimachi, "Crack formation in the continuous casting of steel," *Metallurgical Transactions B*, vol. 8, pp. 489–505, 2 1977.

[16] F. R. Camisani-Calzolari, I. K. Craig, and P. C. Pistorius, "A review on causes of surface defects in continuous casting," *IFAC Proceedings Volumes*, vol. 36, pp. 113–121, 24 2003.

[17] S. G. Concasct, *Beam blanks*, Jan. 2019. [Online]. Available: https://www.sms-concast.ch/our-solutions/caster-concepts/beam-blank.

[18] D. N. Crowther, "The effects of microalloying elements on cracking during continuous casting," *Proceedings of Conference on the Use of Vanadium in Steel*, pp. 99–131, 2001.

[19] M. Y. Demeri, *Advanced high-strength steels: science, technology, and applications*. ASM International, 2013.

[20] R. Dippenaar, S.-C. Moon, and E. Szekeres, "Strand surface cracks-the role of abnormally large prior austenite grains," *Iron & Steel Technology*, vol. 4, pp. 105–115, 2007.

[21] J. Domitner *et al.*, "Modeling the effects of strand surface bulging and mechanical soft reduction on the macrosegregation formation in steel continuous casting," *Metallurgical and Materials Transactions A*, vol. 45, pp. 1415–1434, 3 2014.

[22] J. L. Dosset and H. E. Boyer, *Practical Heat Treating (Second Edition)*. ASM International, 2006, ISBN: 978-1-62708-262-4. DOI: https://doi.org/10.31399/asm.tb.pht2.9781627082624.

[23] P. Du, "Numerical modeling of porosity and macrosegregation in continuous casting of steel," The University of Iowa, 2013.

[24] J. Elfsberg, "Oscillation mark formation in continuous casting processes," Metallernas gjutning, 2003.

[25] V. D. Fachinotti, S. L. Corre, N. Triolet, M. Bobadilla, and M. Bellet, "Two-phase thermo-mechanical and macrosegregation modelling of binary alloys solidification with emphasis on the secondary cooling stage of steel slab continuous casting processes," *International Journal for Numerical Methods in Engineering*, vol. 67, pp. 1341–1384, 10 2006, ISSN: 00295981. DOI: 10.1002/nme.1664.

[26] P. Fan, "Hydrogen pore formation in an al-si alloy - an examination of the role of hydrogen macrosegregation," The University of British Columbia, 2018.

[27] Y. Feng, "3d meso-scale modelling of solidification: Application to advanced high strength steels," McMaster University, 2020.

[28] N. Fonstein, *Advanced High Strength Sheet Steels: Physical Metallurgy, Design, Processing, and Properties*, 1st ed. Springer Cham, 2015, ISBN: 978-3-319-19164-5. DOI: https://doi.org/10.1007/978-3-319-19165-2.

[29] R. Forestier, O. Jaouen, M. Bellet, S. L. Cockcroft, and D. M. M. Editors, "Finite element thermomechanical simulation of steel continuous casting," *Proceedings MCWASP XII, 12th International Conference on Modeling of Casting, Welding and Advanced Solidification Processes*, pp. 295–302, 2009.

[30] A. Ghosh, "Segregation in cast products," *Sadhana*, vol. 26, pp. 5–24, 1 2001.

[31] A. Grajcar, R. Kuziak, and W. Zalecki, "Third generation of ahss with increased fraction of retained austenite for the automotive industry," *Grajcar, A and Kuziak, R and Zalecki, W*, vol. 12, pp. 334–341, 3 2012.

[32] S. Harada, S. Tanaka, H. Misumi, S. Mizoguchi, and H. Horiguchi, "A formation mechanism of transverse cracks on cc slab surface," *ISIJ international*, vol. 30, pp. 310–316, 4 1990.

[33] R. Hardin, P. Du, and C. Beckermann, "Three-dimensional simulation of heat transfer and stresses in a steel slab caster," *Proceedings of the 4th International Conference on Modeling and Simulation of Metallurgical Processes in Steelmaking*, pp. 1–6, 2021.

[34] L. C. Hibbeler, "Multiphysics modelling of the steel continuous casting process," University of Illinois at Urbana-Champaign, 2014.

[35] X. Huang, B. G. Thomas, and F. M. Najjar, "Modeling superheat removal during continuous casting of steel slabs," *Metallurgical Transactions B*, vol. 23, pp. 339–356, 3 Jun. 1992. DOI: 10.1007/bf02656290.

[36] R. M. P. Huitron, P. E. R. Lopez, E. Vuorinen, P. N. Jalali, and M. Kärkkäinen, "Identification of cracking issues and process improvements through plant monitoring and numerical modelling of secondary cooling during continuous casting of hsla steels," *ISIJ International*, vol. 61, pp. 834–843, 3 Mar. 2021, ISSN: 09151559. DOI: 10.2355/ISIJINTERNATIONAL.ISIJINT-2020-442.

[37] ICCT, *Targets for passenger vehicle fuel efficiency in nine countries*, Jul. 2021. [Online]. Available: https://theicct.org/sites/default/files/plot_cafe_pc_SAFE mpg-aug2021.pdf.

[38] T. Inoue and D. Y. Ju, "Analysis of solidification and viscoplastic stresses incorporating a moving boundary: An application to simulation of the centrifugal casting process," *Journal of Thermal Stresses*, vol. 15, pp. 109–128, 1 1992, ISSN: 1521074X. DOI: 10.1080/01495739208946124.

[39] O. B. Isaev, V. V. Kislitsa, and A. V. Fedosov, "Studies of the conditions of formation of transverse corner cracks on the surface of continuous-cast slabs," *Metallurgist*, vol. 55, pp. 720–723, 9 2012, Transverse Crack.

[40] M. I. Khan, M. L. Kuntz, and Y. Zhou, "Effects of weld microstructure on static and impact performance of resistance spot welded joints in advanced high strength steels," *Science and Technology of Welding and Joining*, vol. 13, pp. 294–304, 3 May 2008, ISSN: 13621718. DOI: 10.1179/174329308X271733.

[41] S. Kim, G. Kim, and K. Chin, "Development of high manganese twip steel with 980mpa tensile strength," *International Conference on New Developments in Advanced High-Strength Sheet Steels*, pp. 1–18, 2008.

[42] S. Koric, "Efficient thermo-mechanical model for solidification processes and its applications in steel continuous casting," 2006.

[43] S. Koric, L. C. Hibbeler, and B. G. Thomas, "Explicit coupled thermo-mechanical finite element model of steel solidification," *International Journal for Numerical Methods in Engineering*, vol. 78, pp. 1–31, 1 2009, ISSN: 00295981. DOI: 10.1002/nme.2476.

[44] S. Koric and B. G. Thomas, "Thermo-mechanical model of solidification processes with abaqus," *ABAQUS Users Conference (2007)*, pp. 320–336, 2007.

[45] P. F. Kozlowski, B. G. Thomas, J. A. Azzi, and H. Wang, "Simple constitutive equations for steel at high temperature," *Metallurgical Transactions A*, vol. 23, pp. 903–918, 3 1992. DOI: https://doi.org/10.1007/BF02675567.

[46] J. O. Kristiansson, "Thermal stresses in the early stage of solidification of steel," *Journal of Thermal Stresses*, vol. 5, pp. 315–330, 3-4 1982, ISSN: 1521074X. DOI: 10.1080/01495738208942153.

[47] J. O. Kristiansson, "Thermomechanical behavior of the solidifying shell within continuous-casting billet molds-a numerical approach," *Journal of Thermal Stresses*, vol. 7, pp. 209–226, 3-4 1984, ISSN: 1521074X. DOI: 10.1080/0149573 8408942209.

[48] W. Kurz and D. J. Fisher, *Fundamentals of Solidification*. 1984.

[49] R. Kuziak, R. Kawalla, and S. Waengler, "Advanced high strength steels for automotive industry: A review," *Archives of Civil and Mechanical Engineering*, vol. 8, pp. 103–117, 2 2008, ISSN: 16449665. DOI: 10.1016/s1644-9665(12)6019 7-6.

[50] J. Lait, "Mathematical modelling of heat flow in the continuous casting of steel," *Ironmaking & Steelmaking*, vol. 1, pp. 90–97, 1974.

[51] C. Li and B. G. Thomas, "Thermomechanical finite-element model of shell behavior in continuous casting of steel: Con2d," *Metallurgical and Materials Transactions B*, vol. 35, pp. 1151–1172, 6 2004.

[52] J. Long *et al.*, "Determination of cc slab solidification using nail shooting technique," *Ironmaking & Steelmaking*, vol. 39, pp. 370–377, 5 2012.

[53] R. Mahapatra, J. Brimacombe, I. Samarasekera, N. Walker, E. Paterson, and J. Young, "Mold behavior and its influence on quality in the continuous casting of steel slabs: Part i. industrial trials, mold temperature measurements, and mathematical modeling," *Metallurgical and Material Transactions B*, vol. 22, pp. 861–874, 6 1991.

[54] Z. Malinowski and M. Rywotycki, "Modelling of the strand and mold temperature in the continuous steel caster," *Archives of Civil and Mechanical Engineering*, vol. 9, pp. 59–73, 2 2009, ISSN: 16449665. DOI: 10.1016/s1644-9665(12)60060-0.

[55] E. Manufacturing, *Steel & ahss in automotive: Prominence and impact*, Feb. 2019. [Online]. Available: https://www.industr.com/en/steel-ahss-in-automotive-prominence-and-impact-2361539#.

[56] Market and R. Biz, "Global automotive high strength steel market growth 2022-2028," 2022. [Online]. Available: https://www.marketandresearch.biz/report/235948/global-automotive-high-strength-steel-market-growth-2022-2028.

[57] M. Masarik, L. Čamek, and J. Duda, "Causes of occurrence of internal and surface defects at continuous casting of steel slabs and possibilities of their removal," *Proceedings of 23rd International Conference on Metallurgy and Materials*, pp. 105–110, 2014.

[58] F. Mayer, M. Wu, and A. Ludwig, "On the formation of centreline segregation in continuous slab casting of steel due to bulging and/or feeding," *Steel Research International*, vol. 81, pp. 660–667, 8 2010.

[59] Y. Meng and B. G. Thomas, "Simulation of microstructure and behavior of interfacial mold slag layers in continuous casting of steel," *ISIJ International*, vol. 46, pp. 660–669, 5 2006.

[60] Y. Meng and B. G. Thomas, "Heat-transfer and solidification model of continuous slab casting: Con1d," *Metallurgical and Materials Transactions B*, vol. 34B, pp. 685–705, October 2003.

[61] B. Mintz, "The influence of composition on the hot ductility of steels and to the problem of transverse cracking," *ISIJ International*, vol. 39, pp. 833–855, 9 1999.

[62] D. Paquet, P. Dondeti, and S. Ghosh, "Dual-stage nested homogenization for rate-dependent anisotropic elasto-plasticity model of dendritic cast aluminum alloys," *International Journal of Plasticity*, vol. 27, pp. 1677–1701, 10 Oct. 2011, ISSN: 07496419. DOI: 10.1016/j.ijplas.2011.02.002.

[63] J. K. Park, B. G. Thomas, I. V. Samarasekera, and U. S. Yoon, "Thermal and mechanical behavior of copper molds during thin-slab casting," *Metallurgical and Materials Transactions B*, vol. 33B, pp. 425–449, 2002.

[64] F. Pascon, S. Cescotto, and A. M. Habraken, "A 2.5d finite element model for bending and straightening in continuous casting of steel slabs," *International Journal for Numerical Methods in Engineering*, vol. 68, pp. 125–149, 1 2006, ISSN: 00295981. DOI: 10.1002/nme.1715.

[65] P. Perzyna, "The constitutive equations for rate sensitive plastic materials," *Quarterly of Applied Mathematics*, vol. 30, pp. 321–332, 4 1963.

[66] B. Petrus, K. Zheng, X. Zhou, B. G. Thomas, and J. Bentsman, "Real-time, model-based spray-cooling control system for steel continuous casting," *Metallurgical and Materials Transactions B*, vol. 42, pp. 87–103, 1 2011.

[67] B. Petrus *et al.*, "New method to measure metallurgical length and application to improve computational models," *Iron Steel Technology*, vol. 12, pp. 58–66, 12 2015.

[68] C. Pinheiro, I. Samarasekera, J. Brimacomb, and B. Walker, "Mould heat transfer and continuously cast billet quality with mould flux lubrication part 1 mould heat transfer," *Ironmaking & Steelmaking*, vol. 27, pp. 37–54, 1 2000.

[69] D. A. Porter and K. E. Easterling, *Phase transformations in metals and alloys*. CRC Press, 2009.

[70] O. Richmond and R. Tien, "Theory of thermal stresses and air-gap formation during the early stages of solidification in a rectangular mold," *Journal of the Mechanics and Physics of Solids*, vol. 19, pp. 273–284, 1971.

[71] A. Salpukas, *Technology; continuous casting in steel*, Jan. 1981. [Online]. Available: https://www.nytimes.com/1981/01/01/business/technology-continuous-casting-in-steel.html.

[72] S. Sarna, *Steels for automotive applications*, Oct. 2015. [Online]. Available: https://www.ispatguru.com/steels-for-automotive-applications/.

[73] A. Scholes *et al.*, "Segregation in continuous casting," *Ironmaking & Steelmaking*, vol. 32, pp. 101–108, 2 2005. DOI: https://doi.org/10.1179/irs.2005.32.2.101.

[74] J. Sengupta, M.-K. Trinh, D. Currey, and B. G. Thomas, "Utilization of con1d at arcelormittal dofasco's no. 2 continuous caster for crater end determination," *AISTech 2009 Steelmaking Conference Proc*, pp. 4–9, 2009.

[75] T. Senuma, "Physical metallurgy of modern high strength steel," *ISIJ International*, vol. 41, pp. 520–532, 6 2001.

[76] N. M. Seymour, "Thermo-mechanical behavior of steel in the continuous casting process from meniscus to caster exit," 2016. [Online]. Available: http://hdl.handle.net/2142/92744.

[77] H. Shafy, *Transverse cracking of micro-alloyed steel slabs during continuous casting, handling and charging into the hot strip mill*. Papierflieger, 2021, ISBN: 9783869488066.

[78] M. Shimada and M. Mitsutsuka, "On heat transfer coefficient by forced water cooling to carbon steel," *Tetsu-to-Hagane*, vol. 52, pp. 1643–1650, 10 1966.

[79] J. X. Song, Z. Z. Cai, F. Y. Piao, and M. Y. Zhu, "Heat transfer and deformation behavior of shell solidification in wide and thick slab continuous casting mold," *Journal of Iron and Steel Research, International*, vol. 21, pp. 1–9, 2014.

[80] B. G. Thomas, "Modeling of continuous casting defects related to mold fluid flow," *Congress on Science & Technology of Steelmaking*, vol. 3, pp. 2–17, Apr. 2005.

[81] B. G. Thomas, "Modeling of hot tearing and other defects in casting processes," *Fundamentals of Modeling for Metals Processing*, vol. 22, pp. 362–374, 2009. DOI: 10.31399/asm.hb.v22a.a0005420.

[82] B. G. Thomas, "Review on modeling and simulation of continuous casting," *Steel Research International*, vol. 89, pp. 1–21, 1 2018, ISSN: 16113683. DOI: 10.1002/srin.201700312.

[83] N. Tiedje and E. W. Langer, "Numerical modelling of heat transfer and solidification of continuously cast billets," *Scandinavian Journal of Metallurgy*, vol. 22, pp. 55–60, 2 1993, ISSN: 03710459.

[84] R. H. Tien and V. Koump, "Thermal stresses during solidification on basis of elastic model," *Journal of Applied Mechanics*, pp. 763–767, Dec. 1969.

[85] TRANSVALOR, *Thercast nxt 2.1 user manual continuous casting*, Mougins, France, 2017.

[86] A. Vakhrushev *et al.*, "Norton-hoff model for deformation of growing solid shell of thin slab casting in funnel-shape mold," *Journal of Iron and Steel Research International*, vol. 29, pp. 88–102, 1 Jan. 2022, ISSN: 22103988. DOI: 10.1007/s42243-021-00734-8.

[87] I. Vannier, "Modélisation de la solidification des lingots d'acier," Institut National Polytechnique de Lorraine, 1995.

[88] X. D. Wang, L. W. Kong, M. Yao, and X. B. Zhang, "Novel approach for modeling of nonuniform slag layers and air gap in continuous casting mold.," *Metallurgical and Materials Transactions B*, vol. 48, pp. 357–366, 1 2017.

[89] Y. Wang *et al.*, "Formation and control of transverse corner cracks in the continuous casting slab of a microalloyed steel," *Steel Research International*, vol. 92, pp. 1–11, 6 2021, ISSN: 16113683. DOI: 10.1002/srin.202000649.

[90] Y. Wang, M. Haberkorn, D. Brown, S. Abraham, and R. Petty, "Reduction of transverse corner cracks during continuous casting of slabs," *AISTech - Iron and Steel Technology Conference Proceedings*, vol. 2021-June, pp. 523–533, 2021, ISSN: 15516997. DOI: 10.33313/382/052.

[91] J. H. Weiner and B. Boley, "Elasto-plastic thermal stresses in a solidifying body," *Journal of the Mechanics and Physics of Solids*, vol. 11, pp. 145–154, 3 1963.

[92] J. R. Williams, R. W. Lewis, and K. Morgan, "An elasto-viscoplastic thermal stress model with applications to the continuous casting of metals," *International Journal for Numerical Methods in Engineering*, vol. 14, pp. 1–9, 1 1979.

[93] Y.-M. Won and B. G. Thomas, "Simple model of microsegregation during solidification of steels," *Metallurgical and Materials Transactions A*, vol. 32, pp. 1755–1767, 7 2001.

[94] WorldAutoSteel, *Steel muscle in new vehicles*, 2016. [Online]. Available: https://www.worldautosteel.org/why-steel/steel-muscle-in-new-vehicles/.

[95] WorldAutoSteel, *A new global formability diagram*, Oct. 2021. [Online]. Available: https://ahssinsights.org/blog/a-new-global-formability-diagram/.

[96] J. Wray, "High temperature plastic-flow behavior of mixtures of austenite, cementite, ferrite, and pearlite in plain-carbon steels," *Metallurgical Transactions A*, vol. 15, pp. 2041–2058, 11 1984.

[97] M. Wu, J. Domitner, and A. Ludwig, "Using a two-phase columnar solidification model to study the principle of mechanical soft reduction in slab casting," *Metallurgical and Materials Transactions A*, vol. 43, pp. 945–964, 3 2012.

[98] J. Yang, Z. Xie, Z. Ji, and H. Meng, "Real-time heat transfer model based on variable non-uniform grid for dynamic control of continuous casting billets," *ISIJ International*, vol. 54, pp. 328–335, 2 2014. DOI: https://doi.org/10.2355/isijinternational.54.328.

[99] X. Yang, L. Zhang, C. Lai, S. Li, M. Li, and Z. Deng, "A method to control the transverse corner cracks on a continuous casting slab by combining microstructure analysis with numerical simulation of the slab temperature field," *Steel Research International*, vol. 89, 5 May 2018, ISSN: 16113683. DOI: 10.1002/srin.201700480.

[100] H. Yasunaka, K. Nakayama, K. Ebina, T. SAITO, M. KIMURA, and H. MATUDA, "Improvement of transverse corner cracks in continuously cast hypoperitectic slabs," *Tetsu-to-hagane*, vol. 81, pp. 894–899, 9 1995, Transverse Crack.

[101] D. You, C. Bernhard, G. Wieser, and S. Michelic, "Microsegregation model with local equilibrium partition coefficients during solidification of steels," *Steel Research International*, vol. 87, pp. 840–849, 7 2016.

[102] N. Zabaras, Y. Ruan, and O. Richmond, "Front tracking thermomechanical model for hypoelastic-viscoplastic behavior in a solidifying body," 1990, pp. 333–364.

[103] N. Zabaras, Y. Ruan, and O. Richmond, "On the calculation of deformations and stresses during axially symmetric solidification," *Journal of Applied Mechanics*, vol. 58, pp. 865–871, 1991. [Online]. Available: http://asme.org/terms.

[104] M. L. Zappulla, S. M. Cho, S. Koric, H. J. Lee, S. H. Kim, and B. G. Thomas, "Multiphysics modeling of continuous casting of stainless steel," *Journal of Materials Processing Technology*, vol. 278, p. 116 469, November 2019 2020, ISSN: 09240136. DOI: 10.1016/j.jmatprotec.2019.116469.

[105] M. L. Zappulla and B. G. Thomas, "Surface defect formation in steel continuous casting," *Materials Science Forum*, vol. 941 MSF, pp. 112–117, 2018, ISSN: 16629752. DOI: 10.4028/www.scientific.net/MSF.941.112.

[106] C. Zhang, M. Bellet, M. Bobadilla, H. Shen, and B. Liu, "A coupled electrical-thermal-mechanical modeling of gleeble tensile tests for ultra-high-strength (uhs) steel at a high temperature," *Metallurgical and Materials Transactions A: Physical Metallurgy and Materials Science*, vol. 41, pp. 2304–2317, 9 2010, ISSN: 10735623. DOI: 10.1007/s11661-010-0310-7.

[107] D. Zhang, S. Lei, S. Zeng, and H. Shen, "Thermo-mechanical modeling in continuous slab casting mould and its application," *ISIJ International*, vol. 54, pp. 336–341, 2 2014, ISSN: 09151559. DOI: 10.2355/isijinternational.54.336.

[108] Z. Zhang *et al.*, "Modeling of the as-cast structure and macrosegregation in the continuous casting of a steel billet: Effect of m-ems," *Journal of Materials Processing Technology*, vol. 301, Mar. 2022, ISSN: 09240136. DOI: 10.1016/j.jmatprotec.2021.117434.

[109] W. Zhao and Y. Zhang, "Prediction of transition temperature of alloy steel austenite based on self-organizing neural network," *IOP Conference Series: Materials Science and Engineering*, vol. 563, pp. 1–8, 2 Aug. 2019, ISSN: 1757899X. DOI: 10.1088/1757-899X/563/2/022042.

[110] H. Zhu, "Coupled thermo-mechanical finite-element model with application to initial solidification," 1996.

[111] M. Zucchetti and R. Testoni, "Essays on nuclear technology. volume 1: 2018," Politecnico Di Torino, 2018, ISBN: 9780463877906.